Halogenated Aza-BODIPY dyes for photodynamic anticancer and antimicrobial activity studies

A thesis submitted in fulfilment of the requirement for the degree of

MASTER OF SCIENCE

At

By

TEMLANDVO MATSHIDISO MAGWAZA

DEDICATION

To my late grandmother and dad:

Eva and Maurice

ACKNOWLEDGEMENTS

I would like to express my utmost gratitude to my supervisor Professor J. Mack for his support, assistance, guidance, and patience in conducting this project. His dedication and commitment to ensuring that all his students can achieve the best possible results are unparalleled.

I would also like to thank Distinguished Prof. T. Nyokong deeply for her co-supervision. My sincere gratitude also goes to Ms Gail Cobus for her amazing administrative work and patience with me as I was carrying out this project. I am also extremely grateful to my laboratory S22 colleagues for being supportive throughout the project. The administration and entire staff of the Department of Chemistry gave me tremendous support, which I can never forget. Please also accept my sincere gratitude.

I profusely thank the National Research Foundation (NRF) for granting me adequate financial support and making it possible for me to carry out my work.

Lastly, I would like to thank my sister Thobile, my brother Micheal, and my family and friends that supported me throughout this journey. It was not an easy one, but they always encouraged and supported me even when I lost strength.

WITH THE LORD, EVERYTHING WAS POSSIBLE. I THANK YOU, LORD, FOR YOUR GRACE AND MERCY THROUGHOUT THE JOURNEY OF MY STUDIES

ABSTRACT

This thesis reports on the synthesis and characterisation of differently substituted aza-BODIPY dyes for use in photodynamic antimicrobial chemotherapy (PACT) and photodynamic therapy (PDT) activity studies. The aza-BODIPY dyes were synthesised by adding phenyl and naphthyl rings at the 3,5-positions of the aza-BODIPY core, with methylthiolphenyl (**9a** and **9b**, respectively) or thien-2-yl rings (**9c** and **9d**, respectively) at the 1,7-positions. **9a-c** were iodinated at the 2-position to form **10a-c**, respectively, while **9d** was diiodinated at the 2,6-positions to form **10d**. The methylthiolphenyl-substituted dyes (**10a** and **10b**) were successfully conjugated to gold nanoparticles (AuNPs) to form nanoparticles conjugates (**10a**-AuNPs and **10b**-AuNPs), while attempts to conjugate the thien-2-yl-substituted dyes were unsuccessful. The photophysicochemical properties of **9a-d**, **10a-d** and nanoconjugates **10a**-AuNPs and **10b**-AuNPs were investigated to determine their suitability for use in the applications. Adding heavy atoms such as iodine at the 2,6-positions of the aza-BODIPY led to enhanced singlet oxygen generation since these dyes displayed moderate to high singlet oxygen quantum yields. None of the dyes exhibited any fluorescence.

The PACT activity studies for **9c-d**, **10a-d,** and the **10a**-AuNPs and **10b**-AuNPs were carried out against *Staphylococcus aureus* and *Escherichia coli* with a Thorlabs M660L3 light-emitting diode (LED) with an irradiance of 280 mW/cm^2 for all dyes other than **10d.** A Thorlabs M730L4 LED with an irradiance of 160 mW/cm^2 was used for **10d**. Time dependence studies were only carried out against *Staphylococcus aureus*, so very low log reductions were observed against *Escherichia coli* in initial concentration studies. The **10a**-AuNP and **10b**-AuNP nanoconjugates exhibited high

antimicrobial activity with a log reduction of 9.41 and 0.00% viable colonies, while the iodinated aza-BODIPY had a log reduction of 8.94.

The *in vitro* photodynamic therapy activities and dark cytotoxicity were investigated against human MCF-7 breast cancer cells for dyes **9c-d** and **10c-d** with a Thorlabs M660L3 LED (280 mW/cm^2) for all dyes. The dark cytotoxicity was minimal in each case with IC_{50} > 50. Iodinated dyes **10c** and **10d** had IC_{50} values of 11.6 and 8.2 µM, respectively, and non-iodinated dyes **9c** and **9d** had IC_{50} values of 12.5 and 19.2 µM. The heavy atom effect associated with the iodine atoms increases the singlet oxygen quantum yield and enhances the suitability of the dyes for photodynamic therapy.

Table of Contents

List of Figures

List of Schemes

List of Tables

List of Symbols

A	Absorbance
α	Slope magnitude in singlet oxygen quantum yield calculations
F	Fluorescence
Φ_F	Fluorescence quantum yield
Φ_Δ	Singlet oxygen quantum yield
η	Refractive index
λ	Wavelength
ν	Energy in wavenumbers
$^1O_2$	Singlet oxygen
$^3O_2$	Triplet oxygen
P	Phosphorescence
S_0	Ground state
S_1	Singlet excited state
S_2	Second excited state
T_1	First triplet state
τ_F	Fluorescence lifetime

List of Abbreviations

AuNPs	Gold nanoparticles
Aza-BODIPY	Boron aza-dipyrromethene difluoride
B3LYP	Beck, three-parameters, Lee-Yang-Parr
$BF_3 \cdot OEt_2$	Boron trifluoride diethyl etherate
BODIPY	Boron dipyrromethene difluoride
CAM-B3LYP	Coulomb-attenuated B3LYP
$CDCl_3$	Deuterated chloroform
CFU	Colony forming units
DCM	Dichloromethane
DFT	Density functional theory
DIPEA	*N*,*N*-Diisopropylethylamine
DLS	Dynamic light scattering
DMEM	Dulbecco's modified Eagle's medium
DMSO	Dimethyl sulfoxide
DPBS	Dulbecco's phosphate-buffered saline
DPBF	1,3-diphenylisobenzofuran
DPE	Diphenyl ether

EDX	Energy dispersive X-ray spectroscopy
EPR	Enhanced permeability and retention
FCS	Fetal calf serum
FL-LED	Fluorescence LED
HF	Hartree-Fock
HOMO	Highest occupied molecular orbital
HOMO−LUMO	Energy gap between the HOMO and LUMO
IRF	Instrument response function
ISC	Intersystem crossing
LED	Light emitting diode
LUMO	Lowest unoccupied molecular orbital
MALDI-TOF-MS	Matrix-assisted laser desorption/ionisation-time of flight mass spectrometry
MCF-7	Michigan Cancer Foundation-7 human breast cancer cell line
ML	Medical laser
MOs	Molecular orbital
MS	Mass spectrometry

MTT	3-(4,5-Dimethylthiazol-2-yl)-2,5-diphenyltetrazolium bromide
NBS	*N*-Bromosuccinimide
NIR	Near-infrared
NIS	*N*-iodosuccinimide
NMR	Nuclear magnetic resonance
NPs	Nanoparticles
NRF	National Research Foundation
OA	Oleic acid
OLA	Oleylamine
OPO	Optical parametric oscillator
PACT	Photodynamic antimicrobial chemotherapy
PBS	Phosphate-buffered saline
PDT	Photodynamic therapy
PMT	Photomultiplier tube
PS	Photosensitiser
PTT	Photothermal therapy
ROS	Reactive oxygen species
SDD	Stuttgart Dresden triple zeta effective-core potential

SPR	Surface plasmon resonance
TCSPC	Time-correlated single photon counting
TD-DFT	Time-dependent density functional theory
TEM	Transmission electron microscopy
TLC	Thin-layer chromatography
UV-vis	Ultraviolet-visible
WHO	World Health Organisation
XRD	X-ray powder diffraction
ZnPc	Zinc phthalocyanine

CHAPTER 1

INTRODUCTION

This chapter provides a literature review about photodynamic therapy and photodynamic antimicrobial chemotherapy, the history of aza-BODIPYs, their structures, properties and synthesis, and an introduction to gold nanoparticles, their synthesis, and lastly, the photophysicochemical properties used to characterize the properties of the aza-BODIPY dyes.

1. Introduction

1.1 Photodynamic Therapy

Cancer is one of the most dreaded diseases and is a major cause of mortality, with more than ten million people diagnosed with the disease annually [1]. Cancer kills more people than tuberculosis, malaria, and AIDS combined every year [2]. In 2012, cancer was responsible for 8.2 million deaths worldwide, according to the World Health Organisation (WHO), with around 14 million new cases reported [3,4]. More than 60% of all cases are reported in Africa, Latin America, and Asia [4]. Hence, there is an ongoing need to improve or develop new types of treatments that can address this issue, ideally with none of the side effects associated with traditional treatments such as surgery, chemotherapy, and radiotherapy.

Photodynamic therapy (PDT) is a cancer treatment that has been widely been accepted and adopted, since it improves medical outcomes during the fight against cancer, especially for superficial tumours that are readily accessible with red light from a fibre optic [5]. It is a non-invasive technique developed as an alternative to chemotherapy and surgery [6–8], which provides an alternative treatment for a variety of oncological, dermatological, and cardiovascular diseases due to its potential for selectivity towards cancerous cells. PDT has shown great potential for medicinal use due to its minimised side effects, cost effectiveness and low toxicity towards non-malignant cells [9–14].

PDT relies on three components: a photosensitiser (PS) dye, light irradiation, and molecular oxygen. The PS accumulates selectively in the tumour cells due to the enhanced permeability and retention effect, whereby it react with the reactive oxygen species to destroy the cells [5,14–18]. The photophysicochemical properties of the PS dye dictates the wavelength of light used for PDT and the efficiency with which ground state oxygen can be converted to singlet oxygen. The PS should have the following criteria [15,19–21]:

(i) High selectivity for cancer cells,

(ii) Low toxicity and high biocompatibility,

(iii) Near-infrared light absorption in the therapeutic window (620−850 nm),

(iv) Enhanced ISC and high singlet oxygen quantum yields,

(v) High molar extinction coefficients.

During PDT, the absorption of light by a chromophore generates cytotoxic species, such as singlet oxygen, which leads to irreversible destruction of the treated tissue. The PDT process can follow two different mechanisms:

(i) The Type I mechanism where radicals ($^{\bullet}O_2$ and $^{\bullet}OH$**)** are produced since, in the triplet state, the photosensitiser reacts with substrates that generate radical anion or cation species, which react with molecular oxygen to produce radicals [16].

(ii) The Type II mechanism normally involves energy transfer, whereby in the triplet state, the photosensitiser reacts with molecular oxygen to produce the cytotoxic species ($^1O_2$) [22].

Photodynamic therapy has unique benefits and associated aftereffects. It is less invasive than other treatments, such as surgery, since the PS drug is applied topically or intravenously and more precise since the laser light directly targets the cancer cells. It is usually performed as an outpatient procedure over a short period [23]. The associated aftereffects of PDT are related to the manner in which PS dyes can affect both healthy and unhealthy cells making patients more sensitive to light even after the treatment is complete. It can also cause discolouration of the skin and skin infections [4]. Therefore, the designed photosensitiser must be selective to the tumour cells to avoid damage to normal cells [20].

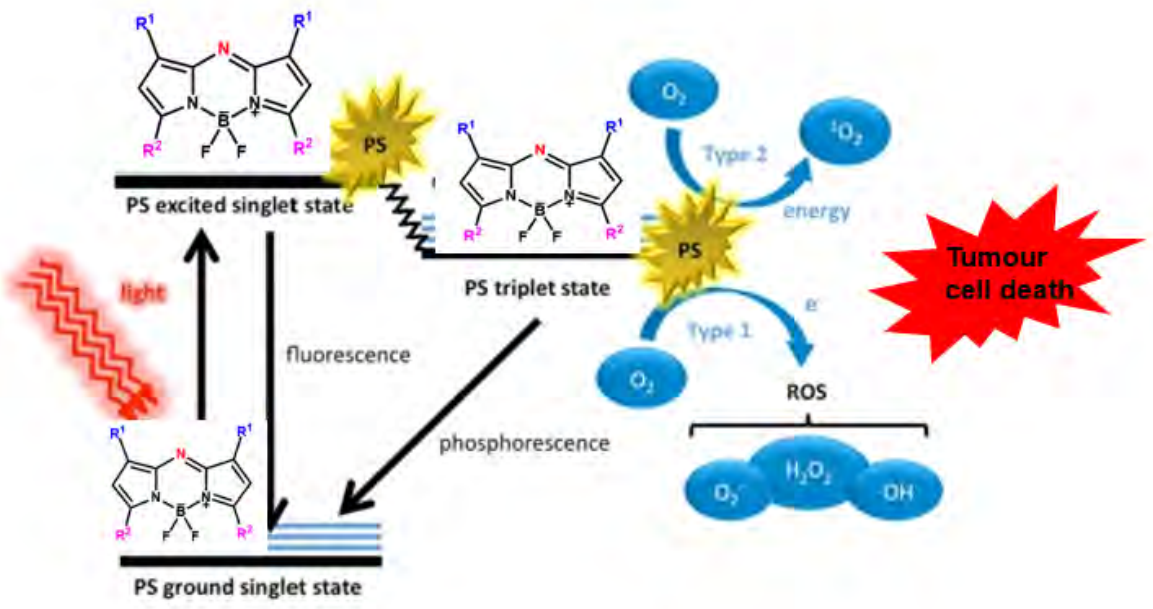

Figure 1.1: A modified Jablonski diagram illustrating the processes involved with PDT. PS = Photosensitiser; ISC = Intersystem crossing; ROS = Reactive oxygen species. Reproduced and modified with permission from Ref. [18]. Copyright © 2012 Frontiers Media.

PDT is ineffective in curing advanced disease since irradiation of the whole body is impossible [24]. The mechanism for generating singlet oxygen and the photochemical processes behind PDT can be explained using the Jablonski diagram (**Figure 1.1**), whereby a photon of light of a specific wavelength absorbed by the ground state of the PS (S_0) to form the first excited state (S_1). The S_1 state can be converted back to the S_0 state via fluorescence through emission of a photon or undergoes intersystem crossing to the long-lived first triplet excited state (T_1). In the triplet manifold, the PS either undergoes phosphorescence to return to the S_0 state by emission of a photon or Type I and Type II electron and energy transfer mechanisms [25–29], whereby the PS interacts with oxygen molecules to generate reactive oxygen radical species and singlet oxygen [5,30,31], which are the cytotoxic agents responsible for the selective destruction of tumour cells during PDT [8,19,26,32–34]. The focus in this project was on investigating the utility of structurally modified aza-tetrarylBODIPY dyes with heavy sulfur and/or iodine atoms (**Figure 1.2**) as the PS dyes in this context.

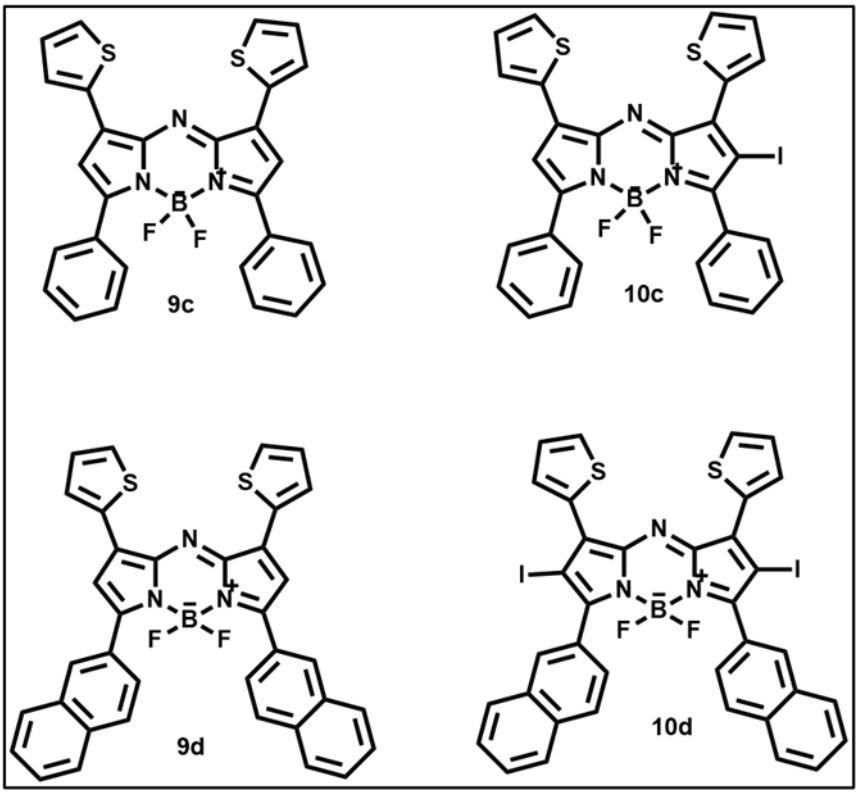

Figure 1.2: Examples of the Aza-BODIPY dyes that have been synthesized for PDT activity studies in this project.

1.2 Photodynamic antimicrobial chemotherapy

A key issue faced by health professionals is the growing resistance of "hospital superbug" bacteria (such as *Staphylococcus aureus* and *Escherichia coli*) to various antibiotics, creating an urgent need to identify new antimicrobial treatments [35]. Photodynamic antimicrobial chemotherapy (PACT) has been applied to the treatment of bacterial infections and as an alternative method for treating drug-resistant pathogens [36]. In a similar manner to PDT, PACT relies on three components: a PS dye, light of a suitable wavelength, and molecular oxygen. The PS must have these properties:

(i) low toxicity,

(ii) high biocompatibility,

(iii) specific release of singlet oxygen.

In a similar manner to PDT, the PS dictates the wavelength of light used and the efficiency with which the ground-state oxygen can be converted to singlet oxygen. During PACT, the absorption of light by a chromophore generates cytotoxic species such as singlet oxygen *via* the Type II mechanism (**Figure 1.3**), which leads to the irreversible destruction of the pathogens [18,37,38].

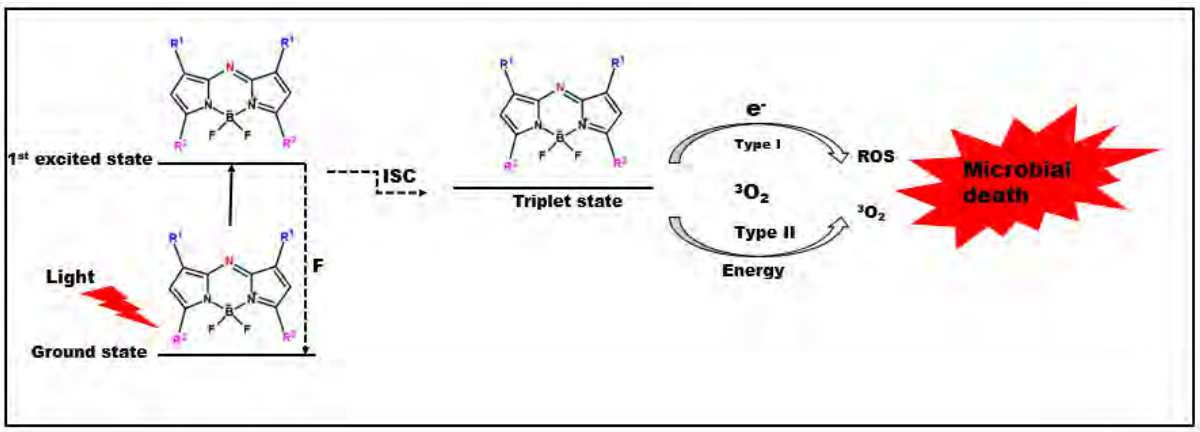

Figure 1.3: Schematic diagram representing the mechanism for the photoinactivation of bacteria during PACT. R^1 and R^2 denote the aryl bands introduced at the 1,7- and 3,5-positions of the aza-BODIPY core. ROS denotes reactive oxygen species formed by the Type I mechanism.

PACT is currently mainly used for oral infections and the disinfection of blood products [36]. It is known to be more effective than antibiotics and/or does not lead to the production of antibiotic-resistant bacterial strains. Antibiotic-resistant bacterial strains such as *Staphylococcus aureus* and *Neisseria gonorrhoea* have been treated with this approach [39]. PACT is a promising alternative to traditional antibiotics due to the ability to sequentially treat microbial infections without the development of

antimicrobial resistance. The efficiency of photoinactivation on PACT depends on the singlet oxygen quantum yields of the dye. PACT is more effective against Gram-(−) and Gram-(+) bacteria, yeasts, and viruses [40]. Gram-(−) bacteria like *Escherichia coli* (*E. coli*) cause various diseases such as urinary tract infection and diarrhoea, and it is known to be less sensitive to photoinactivation as compared to Gram-(+) strain. This is due to the additional cell wall composed of a phospholipid double layer and polysaccharides in the latter [39, 40].

In this study, a series of aza-BODIPY dyes and their gold nanoparticle (AuNP) nanoconjugated were prepared to carry out PACT studies against both *S. aureus* and *E. coli* (**Table 1.1**).

Table 1.1: Aza-BODIPYs that have been used for PACT studies in this study.

	Structure	**Support/NPs**	**Microorganism**
10a	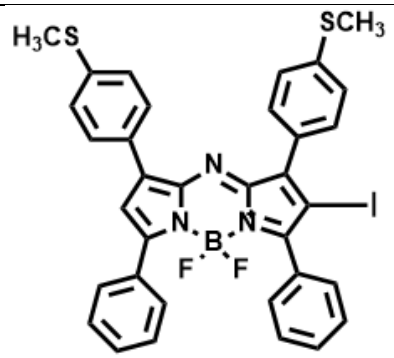	---	*S. aureus*

10b	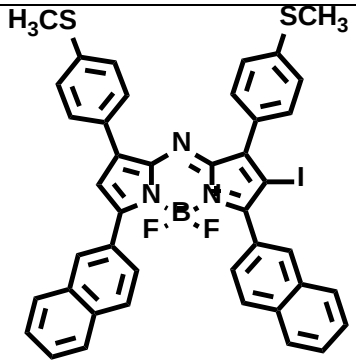	---	*S. aureus*
10a-AuNPs	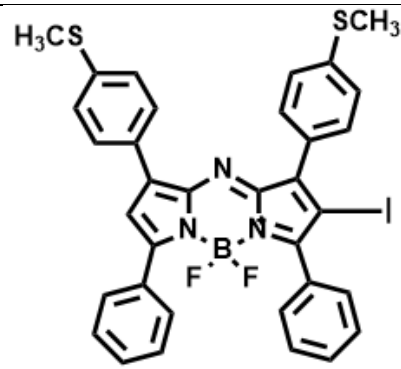	AuNPs	*S. aureus*
10b-AuNPs	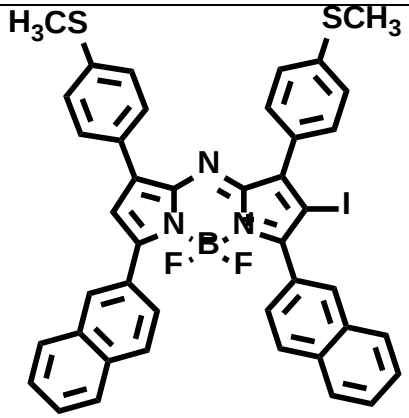	AuNPs	*S. aureus*
9c		---	*S. aureus*

10c	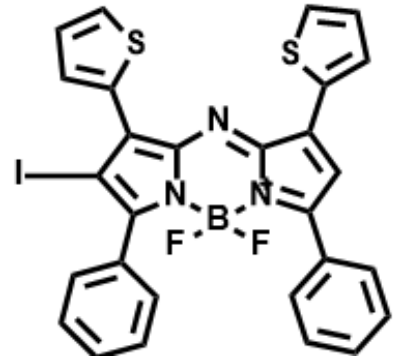	---	*S. aureus*
9d	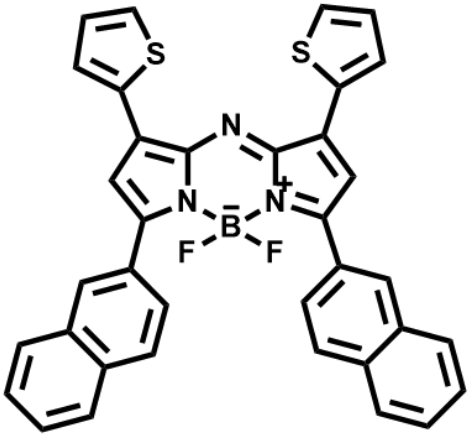	---	*S. aureus*
10d	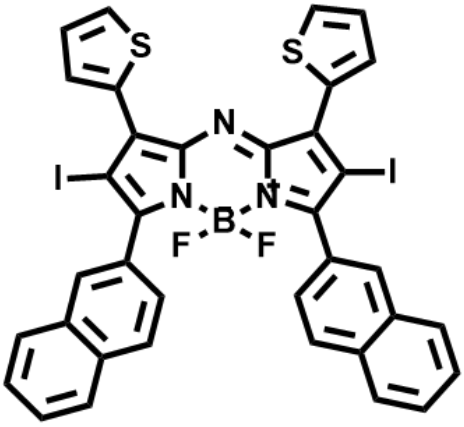	---	*S. aureus*

1.3 Aza-BODIPYs (Boron aza-dipyrromethene difluorides)

BODIPYs are non-aromatic dyes; thus, they do not have Q and B bands since they do not follow Huckel's rule, which states that an aromatic molecule has 4n+2 π-electrons [41,42]. This was caused by introducing BF_2, which then disturbs the aromaticity of the indacene ring system, leading to a complete lifting of the degeneracies of the frontier MOs. BODIPYs are organoboron compounds of particular interest as fluorescent dyes

[43]. Aza-BODIPY dyes are structural analogues of boron dipyrromethene, which were first synthesised in 1993 by Boyer *et al.* [44]. They are composed of an aza-dipyrromethene complexed with a disubstituted boron centre, and structurally aza-BODIPY are derivatives of BODIPY, which are obtained by substituting the *meso*-carbon which connects the pyrrole ring with a highly electron-donating nitrogen atom introduced *via* a Michael addition reaction [45]. **Figure 1.4** shows the molecular structure of aza-BODIPY.

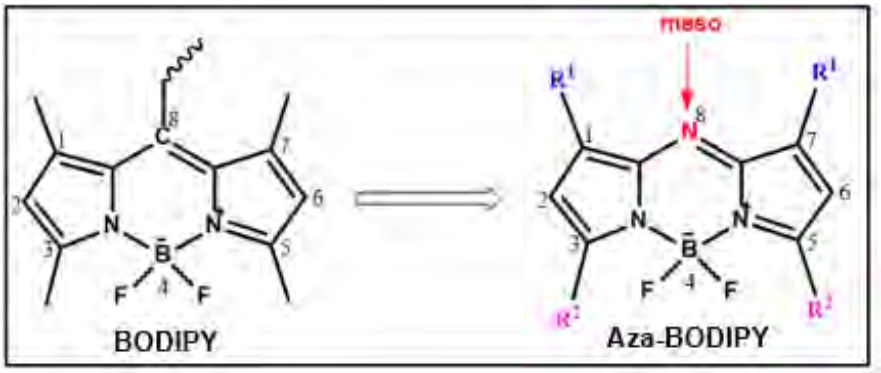

Figure 1.4: Molecular structures of aza-BODIPYs. The numbering system for the BODIPY and aza-BODIPY cores are provided. R^1 and R^2 denote aryl groups that are introduced at the 1,7- and 3,5-positions when the O'Shea method [44] is used. Methyl groups are normally present for BODIPY dyes since 2,4-methylpyrrole is often used as a precursor.

The addition of the nitrogen atom at the bridging position of the aza-BODIPY can shift the main spectral band into the near-infrared (NIR) in the 700−850 nm region when suitable aryl groups are introduced at the 1,3,5,7-positions since this results in a narrowing of the HOMO−LUMO gap, which is not achieved through destabilisation of the HOMO that would make the dyes prone to oxidation [46–48]. The enhanced

stability of the LUMO results in a red shift of the absorption and emission bands into the 620−850 nm region, which is the therapeutic window. **Figure 1.5** illustrates the HOMO and LUMO nodal patterns of the typical aza-BODIPY core structure.

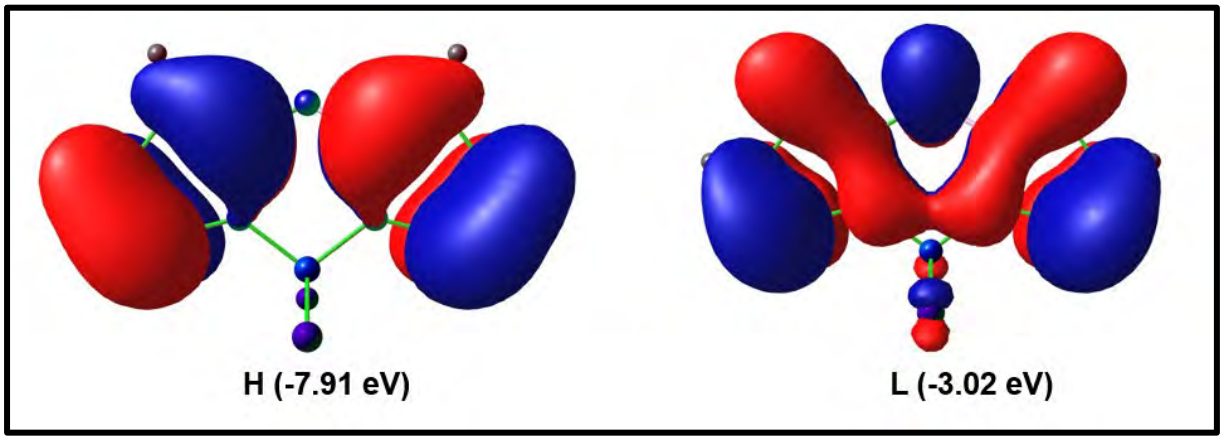

Figure 1.5: Angular nodal patterns of the HOMO (H) and LUMO (L) of the parent aza-BODIPY core dye at an isosurface value of 0.02 a.u.

BODIPY core dyes are visible region fluorescent dyes composed of aza-dipyrromethene complexed by BF_2 [46]. Complexation with BF_2 results in a constrained π-electron tricyclic system which prevents *cis*/*trans* isomerisation of the dipyrromethene ligand [48], allowing conjugation of π-electrons through the carbon-nitrogen backbone so that a rigid structure is formed. Most studies have reported synthetic strategies for the fabrication of these dyes. Recently, the syntheses of symmetric and asymmetric aza-BODIPY dyes have been reported [46,48–50]**.**

Aza-BODIPYs are heteroatom-containing BODIPY analogues, which form a class of near-infrared (NIR) chromophores that absorb strongly in the therapeutic window (620−850 nm). Aza-BODIPYS have different possible applications, such as chemosensors, biomacromolecule labelling, bioimaging, and photodynamic therapy

[51]. These applications are made possible by their physical and chemical properties, which include:

(i) highly rigid molecular structures due to the BF_2 moiety,

(ii) high biocompatibility,

(iii) high luminescent quantum yields depending on substitution properties,

(iv) small Stokes shifts due to the rigid structures,

(v) large extinction coefficients,

(vi) relatively narrow fluorescent emission bands (Φ_F = 0.20−0.40).

Aza-BODIPY shows better photostability than some photosensitisers like cyanine and porphyrins, which enhances their therapeutic efficacy during photodynamic therapy [9,52].

Heavy atoms such as halogens bromine and iodine atoms can be introduced at the 2,6-positions of the aza-BODIPY core, which facilitate the spin-orbital coupling and enhance the spin-forbidden intersystem crossing process [53]. The bromine or iodine atoms help in quenching the fluorescence so that it can enhance the rate of intersystem crossing to the T_1 state, which then reacts with the molecular oxygen to generate singlet oxygen and other reactive oxygen species [5]. These halogen atoms cause both an electron-withdrawing induction and electron-donating mesomeric effects through the interaction of lone pairs of electrons on the halogen atoms with the π-system of the aza-BODIPY core [54,55]. A significant issue faced with aza-BODIPY dyes is their lack of solubility in aqueous solution. In this study, the goal was to prepare aza-BODIPYs with

iodine atoms substituted directly onto the core of the aza-BODIPY at the 2,6-positions to facilitate the most efficient $^1O_2$ generation. Increasing the number of halogen atoms on the aryl rings attached at the 1,3,5,7-positions do not enhance the singlet oxygen quantum yield to the same extent [56–58].

1.3.1 Synthesis

In this section, the general synthetic procedures that are used to prepare aza-BODIPYs and their halogenated derivatives are described.

Aza-BODIPY can be synthesised using the azadipyrromethene derivatives. The azadipyrromethene synthesis was first reported by Rogers in 1943, when tetraarylazadipyrromethene was the first structure to be reported [59]. It was synthesised by heating ammonium formate and a nitroketone in a melt process by using the Leuckart reaction, which gave a low yield. O'Shea and coworkers [44] first synthesised the symmetrical aza-BODIPY using optimised conditions with ammonium acetate and alcohols instead of formate, which helped enhance the yield [59,60] **Scheme 1.1** shows the typical route of how symmetrical aza-BODIPY was synthesised from azadipyrromethene.

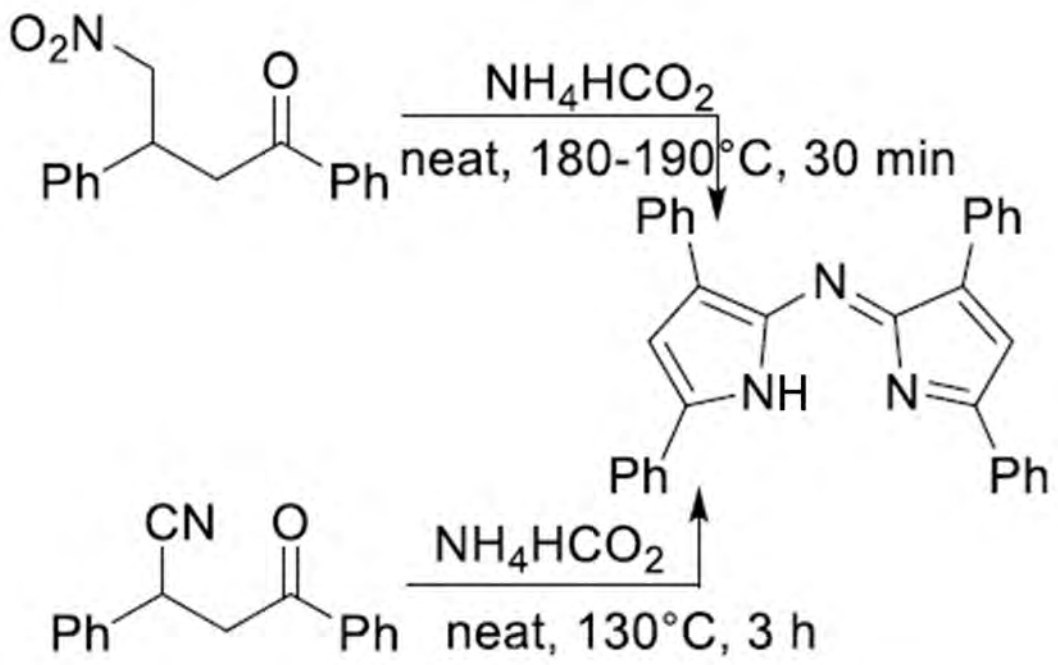

Scheme 1.1: Synthetic pathways that were developed to form azadipyrromethenes by Rogers [59].

Symmetrical aza-BODIPY dye are synthesised by the O'Shea method [44,61] in a series of three reactions, **Scheme 1.2**. A chalcone is prepared from a ketone and an aldehyde through an aldol condensation reaction. The addition of nitromethane through Michael's addition reaction in the presence of a base then yields a nitromethane adduct. Ammonium acetate is added to form an azadipyrromethene core. To obtain an aza-BODIPY from the corresponding azadipyrromethene, a weak organic base is added to remove a pyrrole proton from pyrrole using base *N*,*N*-diisopropylethylamine (DIPEA) and boron trifluoride etherate ($BF_3{\cdot}OEt_2$) at room temperature [62]. The halogenation of the aza-BODIPY core at the 2,6-positions results in the addition of heavy atoms, which enhances the intersystem crossing resulting in the high production of singlet

oxygen. The aza-BODIPY reacted with *N*-iodosuccinimide or *N*-bromosuccinimide at room temperature so that its core could be halogenated.

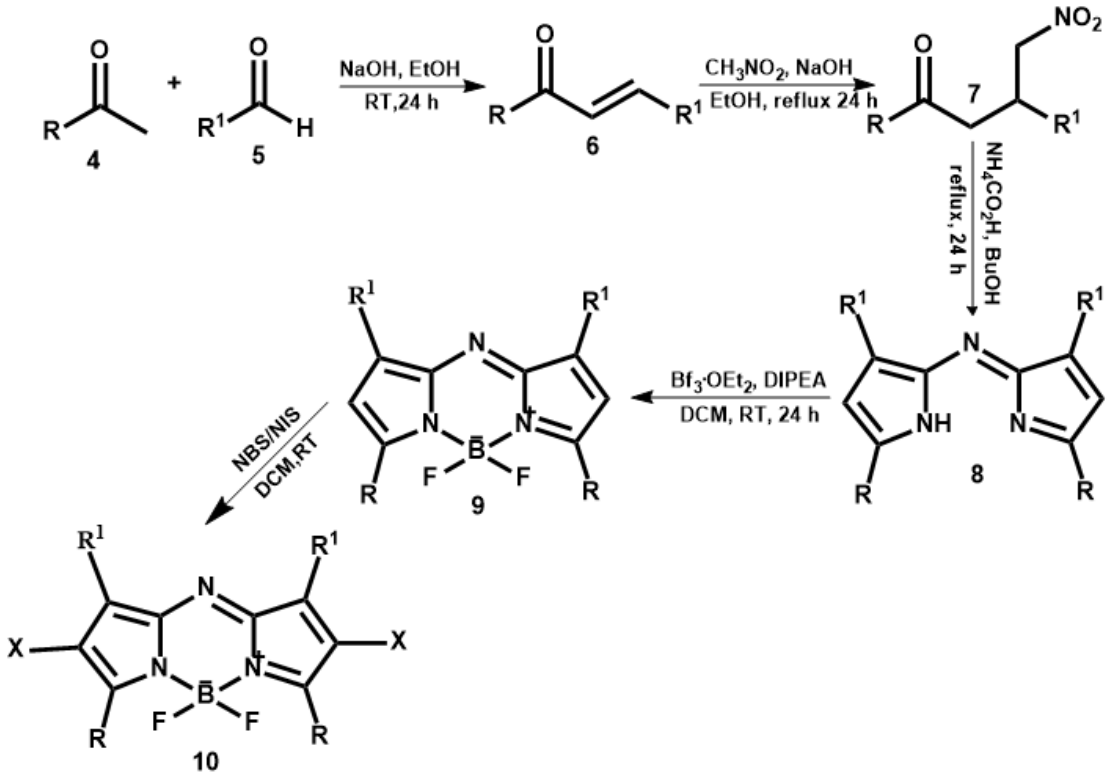

Scheme 1.2: A general synthetic pathway for halogenated aza-BODIPYs.

1.4 Nanoparticles

Nanoparticles are materials that have dimensions in the 1−100 nm range. According to their nanoscale range sizes, they possess physical and chemical properties compared to their bulk counterparts, making them ideal for novel applications [63]. Nanoparticles stem from the family of nanomaterials, which is macromolecular, molecular, and atomic. Nanomaterials are being investigated for the possibility of being used in applications such as medical diagnostics and environmental remediation. Nanoparticles (NPs) will be studied in this project. The physical and chemical properties of NPs are controlled by their composition, size, shape, and crystalline structure. Nanoparticles can

be composed of carbon, metal, metal oxides, and organic matter [64]. Nanoparticles can either occur naturally or can be manufactured. Naturally occurring nanoparticles originate from inorganic or organic compounds, such as metals or polysaccharides. Various nanoparticles like gold, silver, silica nanoparticles and quantum dots are the focus of research, due to the properties they possess [65,66]. The properties include, amongst others, large surface area, enhanced mechanical strength, and stability in chemical processes. Due to these properties, they are applicable in drug delivery, PACT, non-linear optics, imaging, catalysis, and biomedical devices. For drug delivery, nanoparticles are of interest due to their biocompatibility, versatility, improved drug loading, and targeting [67–69]

For this work, gold nanoparticles were adopted for their photothermal effect the enhanced aqueous solubility of nanoconjugates formed with molecular dyes, which are likely to target the cancer cells in PDT, since they have leaky vasculature around the cancer site [70] and also for their enhanced permeability and retention effect (**Figure 1.6**).

1.4.1 Gold nanoparticles

About 2000 years ago, gold nanoparticles (AuNPs) were utilised as pigments for medical and artistic purposes [71]. AuNPs are the focus of considerable interest, especially in the fields of electronics, catalysis, nanobiotechnology, and biosensors, since they have a high active surface area, favourable catalytic properties, and an ability to enhance electrode conductivity [72]. AuNPs have strong absorption bands, due to the surface plasmon resonance (SPR) in the visible range [73]. The position of the SPR band of AuNPs mainly depends on the size and shape of the nanoparticles. Nanospheres

mainly have one SPR band around 530 nm, and nanorods have two absorption bands in the longitudinal and transverse bands [74]. AuNPs have been found to exhibit antimicrobial activity, since they can bind to the bacteria, enhancing photoinactivation, which facilitates the binding of the photosensitiser to the bacteria. AuNPs have the ability to absorb light and convert it to heat through non-radiative processes [22,25,75,76]. These nanoparticles are mostly used in drug delivery since they are inert and non-toxic. They are also known to be effective in photothermal therapy, and they facilitate PDT by increasing the Φ_{Δ} value through an increase in intersystem crossing [77,78]. AuNPs are known to improve dye delivery to the treated tissue due to their enhanced permeability and retention (EPR) effect. They also tend to increase the solubility of the photosensitiser. The prolonged retention of nanocarriers in the cancer cells occurs. The process is known as the EPR and is shown in **Figure 1.6**.

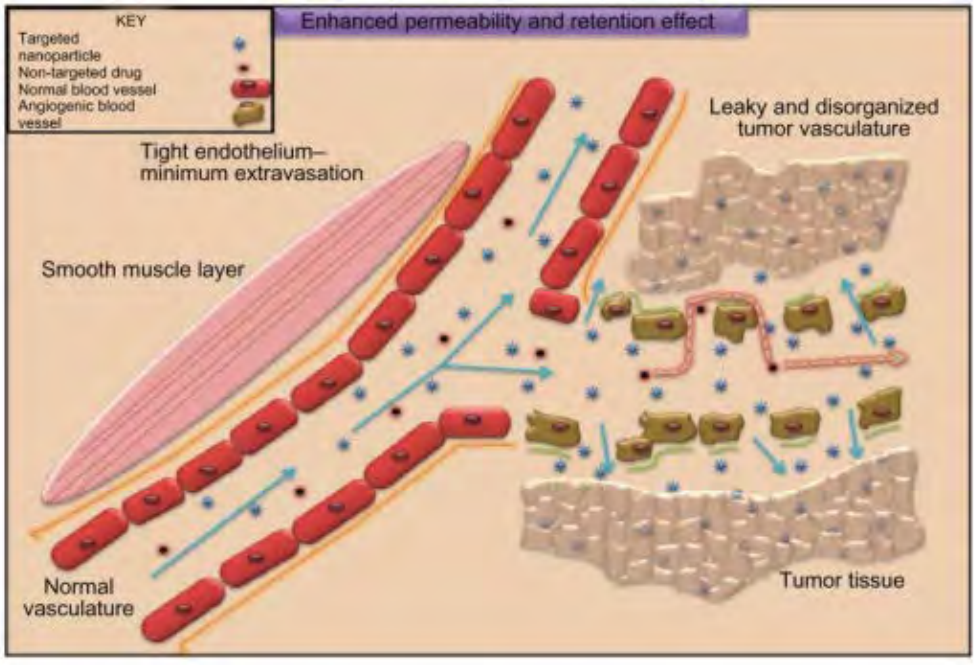

Figure 1.6: The enhanced permeability and retention effect. Reproduced and modified with permission from Ref. [79].Copyright © 2012 Dove Medical Press.

AuNPs can be synthesised using three different approaches, namely biological, chemical, and physical methods. Biological methods utilise plant extracts, bacteria and algae since they contain a chemical which acts as a reducing agent [69,77]. It is advantageous to use biological methods since they are environmentally friendly, cheap, and less toxic [80]. In the context of chemical methods, AuNPs are synthesised by chemical reduction by using inorganic and organic reagents that act as reducing agents. Other chemical methods include the use of micro-emulsions, electrochemical generation and thermal decomposition. Physical methods can use various techniques, including condensation, evaporation, laser ablation and pyrolysis. For this work, AuNPs were synthesised using the chemical method by following procedures reported previously by Mack and coworkers [80] in the context of corrole dyes (**Scheme 1.3**).

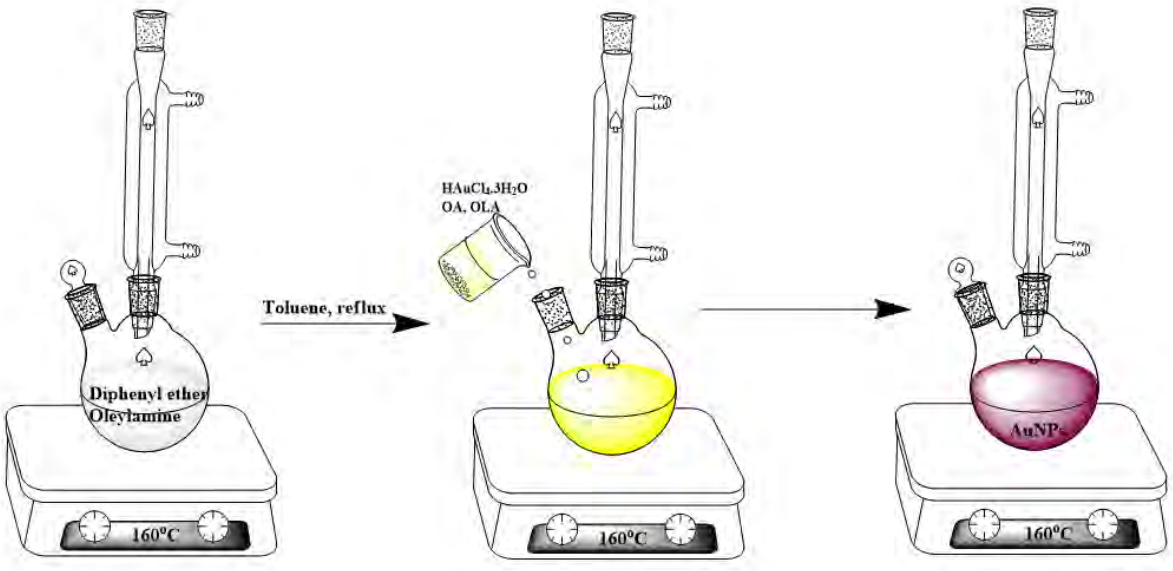

Scheme 1.3: Representation of a typical synthesis of AuNPs [80].

1.5 Photophysical and photochemical parameters

1.5.1 Fluorescence Quantum Yield (Φ_F)

The fluorescence quantum yield (Φ_F) is defined as the ratio of photons emitted through fluorescence to photons absorbed. Φ_F values can be determined by comparing the fluorescence emission intensity observed for the aza-BODIPY dyes with that of a known standard. The fluorescence spectrum is measured with a standard fluorescence emission spectrometer. According to Kasha's rule, fluorescence emission results from the $S_1 \rightarrow S_0$ electronic transition. Typical fluorescence lifetime (τ_F) values for the S_1 state lie on the nanosecond scale. This represents the time that elapses to allow the fluorescence emission intensity to decay to 1/e of its initial value [81]. The related Φ_F and τ_F parameters are important properties of the fluorophores. Attempts were made to determine Φ_F values by using a comparative method that has previously been reported [78,82,83] where the integrated area under the emission spectrum of the PS dye sample solution is compared to that of a standard with a known Φ_F value. In this project, the fluorescence quantum yield of unsubstituted zinc phthalocyanine (ZnPc) was used as a standard in DMSO (Φ_F = 0.20) [84]. The fluorescence quantum yield equation was applied [78,82,83]:

$$\Phi_{F(PS)} = \Phi_{F(Std)} \times \frac{F_{PS} \cdot A_{Std} \cdot \eta_{PS}^2}{F_{Std} \cdot A_{PS} \cdot \eta_{PS}^2} \quad (1)$$

Where F_{PS} and F_{Std} are the areas under the fluorescence curves for the PS dye sample and the standard. A_{PS} and A_{Std} are the absorbance values of the PS dye sample and standard at the excitation wavelength, and η_{PS}^2 and η_{Std}^2 are the refractive indices of the solvent

(DMSO in the context of this study) used for the PS dye sample and the standard measurements.

1.5.2 Singlet Oxygen Quantum Yield (Φ_Δ)

A singlet oxygen quantum yield (Φ_Δ) provides a quantitative measurement of the efficiency with which photosensitisers can use energy in the form of light to convert oxygen in the ground state to the reactive singlet oxygen species, which is useful in photodynamic therapy [85]. The value represents a ratio of the number of singlet oxygen molecules generated to the number of photons absorbed. It can be measured using a comparative chemical method by UV-visible absorption spectroscopy or a with germanium detector to monitor singlet oxygen phosphorescence. Singlet oxygen generation usually plays a role in the application of PDT and PACT. It is normally produced when they reach the T_1 state, where the dye reacts with the molecular oxygen to form singlet oxygen. In this project, the comparative chemical method was used, and calculations were done using methods described in the literature [85,86]. The singlet oxygen quencher used was 1,3-diphenylisobenzofuran (DPBF) in DMSO, which was responsible for monitoring singlet oxygen production in an oxygenated environment [87]. The standard used was methylene blue with $\Phi_\Delta = 0.52$ in DMSO [88]. UV-visible absorption spectroscopy was used to monitor the degradation of the singlet oxygen quencher at the absorption band maximum of DPBF at 419 nm. The singlet oxygen quantum yield equation was applied [85,86]:

$$\Phi_\Delta = \Phi_{\Delta(\mathrm{Std})} \times \frac{\alpha_{\mathrm{Std}}}{\alpha_{\mathrm{PS}}} \qquad (2)$$

Where Φ_{Δ} is the singlet oxygen quantum yield of the PS dye sample, $\Phi_{\Delta(Std)}$ is the singlet oxygen quantum yield of the standard, α_{Std} is the slope value for ΔA against time at the absorption band maximum of the DPBF scavenger for the standard, and α_{PS} is that of the photosensitiser. This equation is only applicable if the refractive index and the optical densities of the standard and PS dye sample solutions are the same.

1.6 Summary of aims

1. Synthesise and characterise aza-BODIPY dyes.
2. Synthesise and characterise AuNPs.
3. Conjugation of aza-BODIPY to nanoparticles by making use of the Au-S affinity and characterisation of the nanoparticle conjugates formed.
4. Evaluating the photophysicochemical properties of the aza-BODIPYs and their nanoconjugates.
5. PACT and PDT activity studies for the synthesised aza-BODIPYs, nanoparticles, and their nanoconjugates.
6. The use of molecular modelling to understand the trends observed experimentally and identify the structural modifications of dyes.

CHAPTER 2

EXPERIMENTAL

This chapter describes the materials, instrumentation, and experimental procedures followed to prepare the aza-BODIPY dyes, gold nanoparticles, and nanoconjugates, and the details of the *in vitro* dark cytotoxicity, PDT and PACT studies.

2. Experimental

2.1 Material

4-(Methythio)benzaldehyde, 2-thiophenecarboxaldehyde, acetophenone, acetonaphthone, sodium hydroxide, nitromethane, sodium carbonate, ammonium acetate, boron trifluoride diethyletherate ($BF_3{\cdot}Et_2O$), iodine, *N*,*N*-diisopropylethylamine (DIPEA), sodium thiosulfate, DPBF, methylene blue, *N*-bromosuccinimide (NBS), *N*-iodosuccinimide (NIS), gold(III) chloride, sodium sulfate, oleylamine, diphenyl ether, sodium chloride and oleic acid were purchased from Sigma Aldrich. Silica gel was used for chromatography columns. Ethanol, ethyl acetate, dichloromethane (DCM), butanol, acetic acid, petroleum ether, toluene, chloroform, deuterated chloroform ($CDCl_3$) and spectroscopic grade dimethyl sulfoxide (DMSO) were obtained from Merck. An Elga Purelab Chorus 2 (RO/DI) system was used to obtain high purity water.

All air- and moisture-sensitive reactions were carried out under argon gas, and dry solvents were used. Cultures of MCF-7 cells were obtained from Cellonex®. Heat-inactivated fetal calf serum (FCS) and 100 unit/mL penicillin-100 μg/mL streptomycin-amphotericin B were obtained from Biowest®. Dulbecco's phosphate-buffered saline (DPBS) and Dulbecco's modified Eagle's medium (DMEM) were obtained from Lonza®. Cell proliferation neutral red reagent (WST-1 assay) and trypan blue were obtained from Sigma-Aldrich. *Staphylococcus aureus* (ATCC) and *E. coli* were obtained from Davies Diagnostics. Phosphate-buffered saline (PBS) solution pH 7.4 was prepared using appropriate amounts of Na_2HPO_4 and NaOH in ultra-pure water

from a Milli-Q Water system (Millipore Corp, Bedford, MA, USA). Nutrient agar and agar bacteriological BBL Muller Hinton broth were purchased from Merck.

2.2 Equipment

- Mass spectra data were collected on a Bruker AutoFLEX III Smart-beam TOF/TOF mass spectrometer using α-cyano-4-hydrocinnamic acid as the MALDI matrix.
- ^{1}H NMR spectra were recorded on a Bruker AMX (600 and 400 MHz) and 80 MHz benchtop NMR spectrometers using deuterated solvent ($CDCl_3$ and C_3H_6O). Non-deuterated CH_2Cl_2 was used for **9c** and **9d** with the 80 MHz benchtop NMR spectrometer, since this is possible with this type of instrument. MestRe Nova was used for data analysis [89].
- Shimadzu UV-2550 and Thermo Scientific Evolution 350 spectrometers were used to measure ultraviolet-visible (UV-vis) absorption spectra with a 1 cm pathlength quartz cuvette.
- Fluorescence emission spectra were measured on a Varian Eclipse spectrofluorimeter with a 1 cm pathlength quartz cuvette.
- Fluorescence lifetime measurements were attempted using a Picoquant® FluoTime 300 time-correlated single photon counting (TCSPC) setup with a Picoquant® LDH-P-485 diode laser (44 ps pulse width, 20 MHz repetition). The fluorescence signal was detected at the magic angle with a Peltier-cooled photomultiplier tube (PMT) module and PicoHarp 300E integrated electronics. The instrument response function (IRF) was measured with a Ludox scattering solution. The data were analyzed using the in-built Picoquant FluoFit software.

- Triplet state lifetimes were determined at 500 nm in N_2 saturated DMSO solutions using an Edinburgh Instruments LP980 spectrometer with a pump beam of 430 nm provided by the optical parametric oscillator (OPO) of an Ekspla NT-342B laser (2.0 mJ / 7 ns, 20 Hz) laser.
- Irradiation for singlet oxygen quantum yield was determined using the Ekspla NT 342B-20AW laser with an Nd:YAG pumping 420-2300 nm optical parametric oscillator (OPO).
- Transmission electron microscopy (TEM) images were obtained using a JEOL TEM 1210 transmission electron microscope at a 100 kV accelerating voltage. TEM samples were prepared by placing a drop of conjugate or nanoparticle solution on the sample grid and allowing it to dry before measurements.
- Dynamic light scattering (DLS) measurements were made on a Zetasizer nano series, Nano-ZS90 instrument.
- Energy dispersive X-ray spectroscopy (EDX) was carried out with an Inca Pentax3 coupled with a Vaga Tescam operated at 20 kV accelerating voltage.
- X-ray powder diffraction (XRD) patterns were recorded on a Bruker D8 Discover instrument equipped with a Lynx Eye Detector, using Cu K_α radiation (λ = 1.5405 Å, nickel filter). Data were collected over a 2θ = 5 to 100° range, scanning at 1° min^{-1} with a filter time constant of 2.5 s per step and a slit width of 6.0 mm. Samples were placed on a zero-background silicon wafer slide. The X-ray diffraction data were treated using Eva (evaluation curve fitting) software. A baseline correction was performed on each diffraction pattern by subtracting

a spline fitted to the curve background. The FWHM values reported in this study were obtained from the fitted curves.

- The theoretical calculations were carried out at the Centre for High Performance computing in Cape Town by using the Gaussian 09 software package to carry out density functional theory (DFT) geometry optimisations at the B3LYP/SDD level of theory, and time dependent-DFT (TD-DFT) calculations were carried out by using the CAM-B3LYP functional with SDD basis sets, to compare the optical properties of the dyes with the experimental spectra. The CAM-B3LYP functional was used since it contains a long-range correction that makes it more suitable for use with dyes that exhibit ICT character
- The MCF-7 cells were cultured in 25 cm^2 vented flasks (Porvair) and then subcultured in 75 cm^2 vented flasks (Porvair) in a humidified atmosphere incubator with 5% CO_2 at a physiological temperature of 37°C (Heal Force). 3-(4,5-Dimethylthiazol-2-yl)-2,5-diphenyltetrazolium bromide (MTT) cell proliferation neutral yellow reagent was used to measure the cell viability through a Synergy 2 multi-mode microplate reader (BioTek®). PDT studies were conducted using a Modulight® Medical Laser system (ML) 7710−680 fitted with a Thorlabs M660L3 light-emitting diode (LED).
- The optical density of the bacteria culture was determined using the Ledetect 96 microplate reader from Labxim Products.
- A China Medical Device RAU-530D autoclave was used to sterilise and autoclave nutrient broth, agar, PBS buffer, and the apparatus used for the bacterial and cancer studies.

- A Vortex mixer from Lasiec was used to mix the bacteria suspension.
- A Hermle Z233M-2 centrifuge from Lasiec was used to harvest bacteria from the suspension.
- The thermostatic oven was used for the incubation processes for the photodynamic antimicrobial chemotherapy.
- A Scan® 500 automatic colour colony counter was used to determine the colony-forming units (CFU)/ml values of the bacteria.
- A Zeiss-AxioVert fluorescence LED (FL-LED) inverted microscope was used to view the cells under phase contrast.

2.3 Synthesis

2.3.1 Synthesis of aza-BODIPY

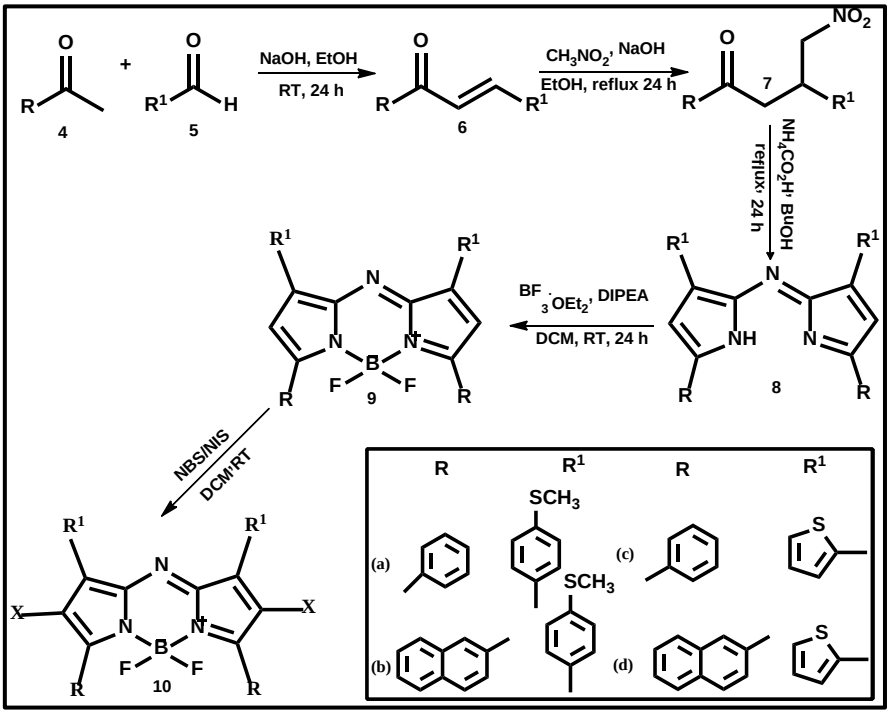

Scheme 2.1: Synthetic pathway for the aza-BODIPY dyes. The inset provides the rings introduced at the 3,5- (R) and 1,7- (R^1) positions.

Aza-BODIPYs (**Scheme 2.1**) were prepared following the general synthesis procedure. The aldehyde and ketone were dissolved in ethanol (1:1 mol equiv.), and base (NaOH) was added to stir for 24 h at room temperature. Chalcone was crystallised by pouring the mixture over ice, and the pH was adjusted by using hydrochloric acid (HCl). It was then recrystallised using MeOH, filtered and allowed to dry. Obtaining the nitromethane adduct chalcone was dissolved in ethanol, 3-4 pellets of NaOH were added, and the mixture was degassed for 30 min. Nitromethane (5 mol equiv.) was added under an inert atmosphere letting the reaction mixture reflux for 24 h. The reaction was monitored using thin-layer chromatography (TLC) since the UV-visible absorption spectroscopy did not provide enough data. The mixture was washed with DCM and brine water and dried with sodium sulfate. The nitromethane adduct was dissolved in butanol/glacial acetic acid (3:1) and degassed for 1 h. Ammonium acetate (30 mol equiv.) was added to form azadipyrromethene. TLC was used to monitor the progress of the reaction to completion. The reaction mixture was washed with DCM and Millipore water and dried with sodium sulfate to remove excess water. The product was purified by silica gel column using solvent system petroleum ether and ethyl acetate (9:1). The azadipyrromethene was dissolved in dry DCM, and base DIPEA (10 mol equiv.) was added and stirred at 30°C for 10 min to achieve chelation with BF_2. $BF_3 \cdot OEt_2$ (45 mol equiv.) was added dropwise, and the reaction was stirred for 24 h. UV-visible absorption spectroscopy and TLC were used to monitor the reaction to completion. The product was purified by silica column chromatography using petroleum ether: ethyl acetate, THF, and chloroform. The solvent was removed with a rotary evaporator.

*Halogenation of aza-BODIPY **10a-d***

Aza-BODIPY was dissolved in a solvent system chloroform, and glacial acetic acid (3:1) and NIS (2.5 mol equiv.) were added under an inert atmosphere. The reaction was monitored using UV-visible absorption spectroscopy to observe the spectral shift and TLC to see if it had reached completion. The resultant product was purified by silica gel column chromatography using DCM or chloroform.

Physiochemical properties of synthesized dyes

9c was obtained in 35% yield; UV-vis (DMSO) λ / nm 682; ^{1}H NMR (80 MHz, CH_2Cl_2) δ 8.07 (d, *J* = 3.0 Hz, 1H), 7.96 (dd, *J* = 3.6, 1.2 Hz, 2H), 7.64 (d, *J* = 1.1 Hz, 1H), 7.57 (d, *J* = 1.1 Hz, 2H), 7.51 (d, *J* = 3.2 Hz, 3H), 7.43 (d, *J* = 3.2 Hz, 2H), 7.36 (d, *J* = 0.5 Hz, 2H), 7.23 (d, *J* = 1.4 Hz, 1H), 7.18 (s, 1H), 6.94 (d, *J* = 1.3 Hz, 2H), 6.76 (s, 1H). MS (MALDI-TOF): [$C_{28}H_{18}BF_2N_3S_2$] Anal. calc. *m*/*z* 509.40*;* Found: $[M]^+$ 509.31.

9d was obtained in 40% yield; UV-vis (DMSO) λ / nm 708; ^{1}H NMR (80 MHz, CH_2Cl_2) δ 8.72 (d, *J* = 1.5 Hz, 1H), 8.58 (d, 1H), 8.38 (d, *J* = 1.9 Hz, 3H), 8.16 (d, *J* = 1.9 Hz, 1H), 8.06 (d, *J* = 2.0 Hz, 1H), 7.95 (d, *J* = 2.3 Hz, 1H), 7.84 (d, 1H), 7.81 (d, *J* = 3.2 Hz, 1H), 7.59 (d, *J* = 2.7 Hz, 5H), 7.47 (d, *J* = 2.2 Hz, 1H), 7.30 (d, 1H), 7.25 (d, *J* = 1.3 Hz, 1H), 7.13 (d, 1H), 7.00 (d, *J* = 0.9 Hz, 1H), 6.63 (s, 1H), 6.43 (s, 1H). MS (MALDI-TOF): [$C_{36}H_{22}BF_2N_3S_2$] Anal. calc. *m*/*z* 609.13*;* Found: $[M]^+$ 608.42.

10a was obtained in 62% yield; UV-vis (DMSO) λ / nm 663; MS ^{1}H NMR (400 MHz, $CDCl_3$) δ 8.21 (d, *J* = 1.6 Hz, 2H), 8.19 (d, *J* = 1.2 Hz, 2H), 7.93 (s, 1H), 7.91 (d, *J* = 2.4 Hz, 3H), 7.83 (d, *J* = 8.2 Hz, 2H), 7.56 (d, *J* = 1.5 Hz, 1H), 7.54 (d, *J* = 1.8 Hz, 2H), 7.52 (d, *J* = 2.4 Hz, 2H), 7.50 (d, *J* = 1.3 Hz, 2H), 7.47 (d, *J* = 7.2 Hz, 2H), 2.81 (s, 6H). (MALDI-TOF):[$C_{33}H_{25}BF_2N_3S_2$] Anal. calc. *m*/*z* 715.42; Found: $[M]^+$ 715.84.

10b was obtained in 78% yield; UV-vis (DMSO) λ / nm 690; ^{1}H NMR (80 MHz, C_3H_6O) δ 8.39 (s, 1H), 8.10 (s, 1H), 8.00 (d, J = 1.8 Hz, 3H), 7.83 (s, 1H), 7.76 (s, 1H), 7.57 (d, J = 2.7 Hz, 2H), 7.46 (s, 5H), 7.36–7.35 (m, 4H), 7.14–7.04 (m, 2H), 6.98 (d, J = 2.4 Hz, 2H), 2.26 (s, 6H). MS (MALDI-TOF):[$C_{38}H_{29}BF_2N_3S_2$] Anal. calc. *m*/*z* 815.54; Found: $[M]^+$ 816.21.

10c was obtained in 45% yield; UV-vis (DMSO) λ / nm 677; ^{1}H NMR (80 MHz, $CDCl_3$) δ 8.07 (s, 1H), 7.96 (d, *J* = 1.1 Hz, 2H), 7.91 (d, *J* = 1.1 Hz, 1H), 7.62 (d, *J* = 1.1 Hz, 2H), 7.55 (d, *J* = 1.0 Hz, 1H), 7.51 (s, 2H), 7.47 (s, 2H), 7.43 (s, 1H), 7.21 (d, *J* = 1.3 Hz, 2H), 7.16 (s, 1H), 6.91 (s, 2H); MS (MALDI-TOF): [$C_{28}H_{17}BF_2N_3S_2$] Anal. calc. *m*/*z* 635.30; Found: $[M]^+$ 635.66.

10d was obtained in 52% yield; UV-vis (DMSO) λ / nm 707; ^{1} H NMR (600 MHz, $CDCl_3$) δ 8.68 (s, 1H), 8.57 (s, 1H), 8.42 – 8.36 (m, 3H), 8.16 (d, *J* = 1.9 Hz, 1H), 8.06 (d, *J* = 2.0 Hz, 1H), 7.95 (d, *J* = 2.3 Hz, 1H), 7.83 (t, *J* = 8.4 Hz, 1H), 7.74 – 7.67 (m, 1H), 7.58 (d, *J* = 2.7 Hz, 1H), 7.61 – 7.47 (m, 5H), 7.49 – 7.48 (m, 2H), 7.22 (dd, *J* = 6.2, 2.4 Hz, 1H), 7.03 (d, *J* = 10.7 Hz, 1H).MS (MALDI-TOF): [$C_{36}H_{20}BF_2N_3S_2$]Anal. calc. *m*/*z* 861.20*;* Found: $[M]^+$ 863.12.

In contrast with **9c** and **9d**, the non-iodinated analogues of **10a** and **10b** were not purified and characterised, since they were only used to prepare **10a** and **10b**.

2.3.2 Synthesis of AuNPs

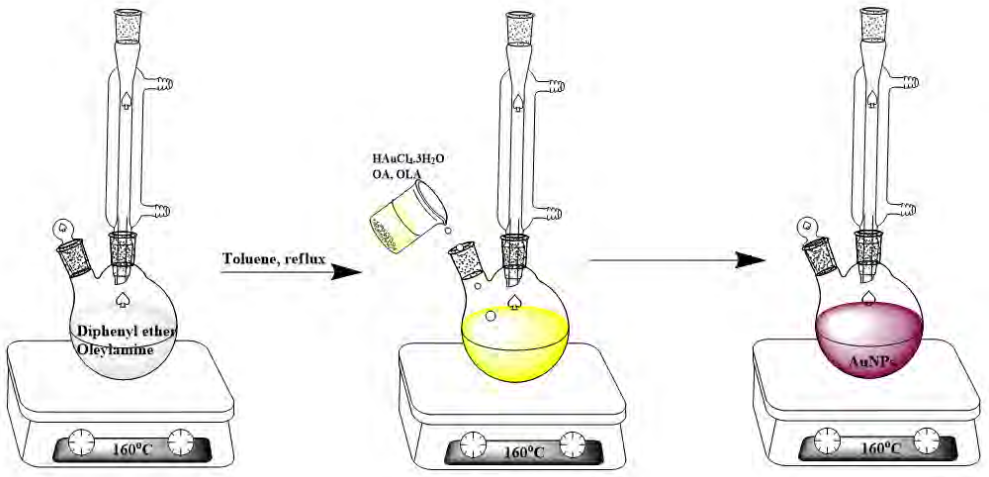

Scheme 2.2: Synthetic route used to prepare the AuNPs.

The synthesis of AuNPs (**Scheme 2.2**) was achieved by following a previously reported procedure in the literature [80]. Briefly, 10 mL diphenyl ether, 2 mL oleylamine, and toluene were refluxed at 160°C in a 50 mL round bottom flask. 50 mg gold salt was dissolved in 2 mL toluene, 2 mL oleic acid, and 2 mL oleylamine. The gold salt solution was added to the refluxing mixture all at once, and a pale yellow to wine-red colour was observed. The solution was cooled down and then washed with ethanol. The precipitate was collected by centrifuge for 20 min at 3000 rpm.

2.3.3 Conjugation of aza-BODIPY to AuNPs

The conjugation of aza-BODIPY to AuNPs (**10a** and **10b**).

The **10a**-AuNP and **10b**-AuNP nanoconjugates were synthesised using the same procedure but treated differently by adding **10a**/**10b** (10 mg) dissolved in 5 ml of toluene into 20 mL round bottom flask, followed quickly by AuNPs (4 mg) in 2 mL of toluene. After 2 h of further heating at reflux, the solution was stirred at room temperature for 24 h. The conjugate was precipitated out of the solution using methanol

by centrifugation at 3000 rpm for 20 min. These products were washed with methanol and ethanol to remove the unreacted **10a** or **10b**. Referring to **Scheme 2.3**, the linkage of nanoparticles to the aza-BODIPYs **10a** and **10b** occurs *via* non-covalent, which is the Au-S interaction caused by the high sulfur affinity of the atoms [90].

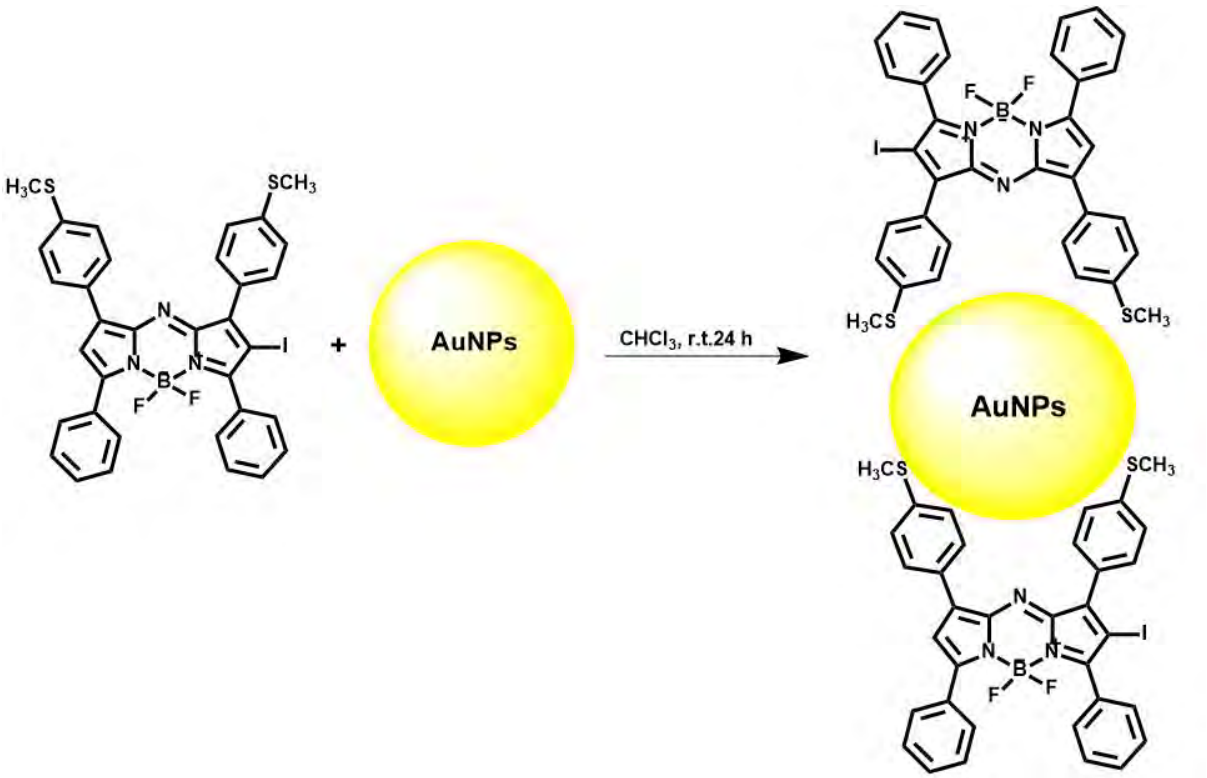

Scheme 2.3: The conjugation of **10a** to AuNPs.

2.4 Experimental conditions for the photophysicochemical studies

For the Φ_{Δ} measurements, DPBF was used as a quencher and was initially prepared with an absorbance of 2.0 at 419 nm. Equal volumes of 1.5 mL of azaBODIPY PS dye or standard solution and quencher were mixed and the solution was irradiated at the absorption maxima of the main spectral band of the dye. UV-visible absorption spectra were recorded and were used to monitor the degradation of DPBF at 30 s intervals in terms of the photoirradiation at a crossover wavelength for the sample and standard solutions.

For the Φ_F measurements, all the optical densities were fixed at 0.05 to avoid any inner filter effect. Both the standard and the sample were excited at the same crossover wavelength. No fluorescence was observed for any of the dyes and the nanoparticle conjugates in either DMSO or DCM.

For the τ_T measurements, the experiments were performed using a 1 cm quartz cell filled with the aza-BODIPY solution in DMSO, which was then degassed using argon to remove any oxygen. The absorbance of the standard and sample was adjusted to 1.5 at their crossover wavelength.

2.5 Antimicrobial studies

The microorganisms used were *S. aureus* and *E. coli*, which were grown on agar plates according to the manufacturer's specification to obtain an individual colony. The bacteria culture was prepared following the procedure described in the literature [91]. Briefly, aliquots of the culture were transferred to 4 mL of fresh broth and incubated at 37°C to obtain a mid-logarithmic phase ($OD_{620\ nm} \approx 0.6$). The bacteria in the growth logarithmic phase were harvested through broth culture removal by centrifugation (3000 rpm for 15 min) and washed three times in PBS. The bacteria culture was diluted to 1/1000 in PBS as the working stock solution, corresponding to approximately 10^8 colony-forming units (CFU) per mL.

PACT activities of bacteria were performed using a previously reported method [91]. In all the experiments, *S. aureus* and *E. coli* suspensions were incubated in an oven with a shaker for 30 min at 37°C. Then 3 mL of the incubated bacteria suspension was irradiated at the absorption maxima of the main spectral band of the photosensitisers in

24 well plates using the illumination kit of a Modulight® 7710−680 Medical Laser fitted with a Thorlabs M660L3 LED with an irradiance of 280 mW/cm^2 (measured with a Coherent FieldmaxII TOP energy/power meter fitted with a Coherent Powermax PM10 sensor) for all dyes and nanoconjugates except **10d** and the other 3 mL was kept in the dark. A Thorlabs M730L4 LED with an irradiance of 160 mW/cm^2 was used for **10d**. After irradiation, 100 µL samples were inoculated on the agar plate, and the plates were incubated at 37°C for 20 h. The experiments were done in triplicates.

2.6 Photodynamic Studies

2.6.1 *In vitro* dark cytotoxicity

Cell culturing and *in vitro* studies were carried out following procedures reported previously in the literature [92,93]. *In vitro* cytotoxicity studies were carried out in the dark by using human breast adenocarcinoma (MCF–7) cells. The MCF-7 cells were cultured using DMEM containing 4.5 g/L glucose with L-glutamine and Phenol red, supplemented with 10% (v/v) heat-inactivated FCS and 100 unit/mL penicillin-100 µg/mL streptomycin-amphotericin B. The cells were grown in 75 cm^2 vented flasks (Porvair) and incubated at 37°C and 5% CO_2 in a humidified atmosphere. The cells were rinsed with DPBS and lifted with trypsin. Viable trypsinised cells were counted with a hemocytometer. 10,000 cells/well were seeded in supplemented DMEM containing phenol red in 96-well tissue culture plates (Porvair®). The cells were incubated at 37°C under a 5% CO_2 atmosphere for 24 h to facilitate cell attachment to the wells. The cells adhered to the wells were washed with 100 µL DPBS twice, followed by the addition of 100 µL supplemented DMEM for aza-BODIPYs **9c**, **9d**, **10c**, and **10d** at a range of different concentrations (0, 2.5, 5, 10, 20, 30, 40 and 50 µM).

After 24 h treatment, the wells were rinsed with 100 μL DPBS twice, supplemented DMEM and phenol red were added, and the plates were re-incubated for 24 h. Quantification was conducted using a Synergy 2 multi-mode microplate reader (BioTek®) by following the manufacturer's instructions. The percentage cell viability (% Cell viability) was determined using Eq. (3):

$$\% \text{ Cell Viability} = \frac{Absorbance\ of\ sample\ at\ 450\ nm}{Absorbance\ of\ control\ at\ 450\ nm} \times 100 \quad (3)$$

Where Absorbance of sample at 450 nm is the absorbance value for the cells containing the photosensitiser dye, whereas Absorbance of control at 450 nm is the value for the placebo cells containing only supplemented DMEM with phenol red.

2.6.2 *In vitro* photodynamic therapy

The MCF-7 cells treated for PDT were cultured and seeded into 96-well plates, as described in the previous section. The stock concentrations of aza-BODIPY dyes **9c**, **9d**, **10c,** and **10d** were prepared in 1% DMSO, and the volume was made up of supplemented DMEM. Placebo cells were incubated with supplemented DMEM only. After 24 h treatment, the wells were washed twice with 100 μL DPBS, supplemented DMEM with Phenol red was added, and the plates were re-incubated for 24 h. The plates were washed with 100 μL PBS and Phenol red-free supplemented DMEM was added instead of supplemented DMEM with phenol red. The MCF-7 cancer cells were plated in 96 wells, treated with the compounds, and irradiated for 20 min using the illumination kit of a Modulight® 7710−680 Medical Laser fitted with a Thorlabs M730L4 LED for **10d** and a Thorlabs M660L3 LED for **9c**, **9d** and **10c** with irradiance values of 160 and 280 mW/cm^2 (measured with a Coherent FieldmaxII TOP

energy/power meter fitted with a Coherent Powermax PM10 sensor), respectively. After irradiation, the medium was replaced with supplemented DMEM containing phenol red. The culture medium was discarded, and 200 μL of DMSO was added to dissolve the purple formazan crystals. A Synergy 2 multi-mode microplate reader (BioTek®) was used to determine the number of viable cells after treatment at an excitation wavelength of 540 nm. The cytotoxicity of the compounds was measured as the percentage ratio of the absorbance of the treated cells to the untreated controls.

2.6.3 Cellular drug uptake

Cellular drug uptake over 24 h was determined for **9c**, **9d**, **10c** and **10d**. Cells were grown in a 96 well-plate and inoculated with aza-BODIPY dyes at concentrations of 0, 2.5, 5, 10, 20, 30, 40, and 50 μM in 1% DMSO/culture media and control sample prepared in 1% DMSO/culture media. The plate was incubated at 37 ºC under a 5% CO_2 atmosphere for 24 h. After incubation, cells were washed twice with PBS to remove any compound that had not been absorbed into the cells. Cells were solubilised in 100 μL of 30% Triton X-100 in PBS. The cell-accumulated aza-BODIPY dye was detected by fluorescence using an ELISA reader with excitation and emission wavelengths of 660 and 680 nm, respectively.

2.7 Attempted syntheses

Conjugation of the thien-2-yl sulfur atoms of **10c** and **10d** to AuNPs was unsuccessful (**Scheme 2.4**), as were attempts to brominate **10c** and **10d** (**Scheme 2.5**). The original target compounds for **10a-c** were the diioidinated rather than the monoiodinated dyes. It was concluded that NIS was not sufficiently reactive in this context, so attempts were made to use iodine for the iodination reaction instead. MS data made it clear that it was

not just the 2,6-positions that were iodinated in this context. No attempt was made to separate the complicated mixtures of products formed in this context, so the decision was made to study the PDT and/or PACT activities of **10a-c** and compare them with those of **10d**. No further attempt was made to prepare the diiodinated target compounds.

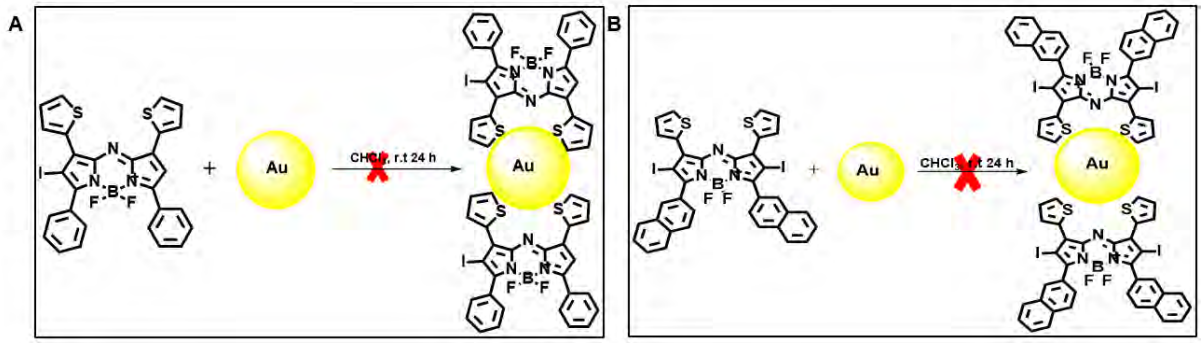

Scheme 2.4: The attempted conjugation of (A) **10c** and (B) **10d** to AuNPs.

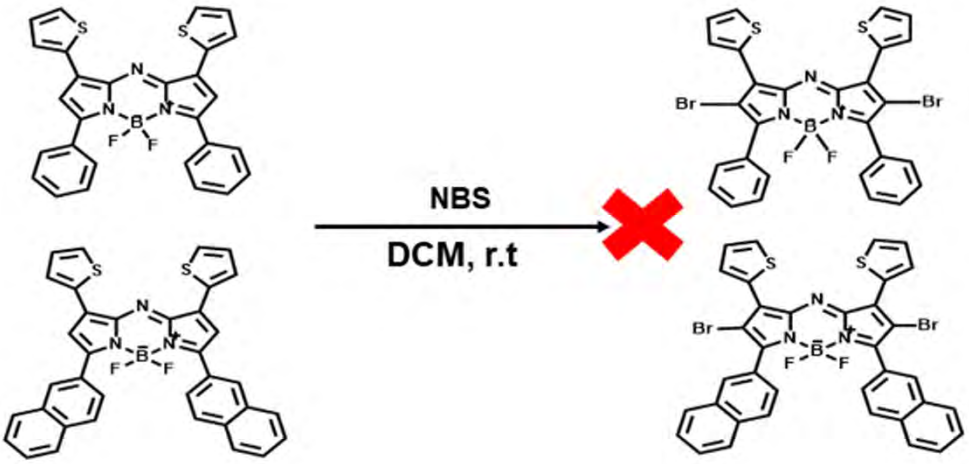

Scheme 2.5: The attempted bromination of **10c** and **10d**.

2.8 Concluding remarks

The aza-BODIPY dyes were successfully synthesised using synthetic routes reported previously in the literature. Mass spectrometry and ^{1}H NMR spectroscopy were the main instrumental techniques used to confirm the successful syntheses.

CHAPTER 3

SYNTHESIS. CHARACTERISATION AND PHOTOPHYSICOCHEMICAL PROPERTIES OF THE AZA-BODIPY DYES

This chapter discusses the synthesis and characterisation of the aza-BODIPY dyes. UV-visible absorption spectroscopy, mass spectrometry, and nuclear magnetic resonance spectroscopy were used to characterise the dyes.

3. Synthesis and characterisation of aza-BODIPY dyes

3.1.1 Synthesis of aza-BODIPY (9c-d and 10a-d) dye

The synthesis of halogenated aza-BODIPY was achieved using the procedure shown in **Scheme 3.1**, where it was done by first preparing the azadipyrromethene, then by complexing it and adding heavy atoms. The azadipyrromethene was achieved using the three-step route, whereby a selected aldehyde and ketone are added to ethanol in the presence of NaOH(base). Michael's addition of nitromethane to the chalcone results in 1,3-diaryl-4-nitrobutan-1-one **7** in the presence of NaOH (base). Condensation with ammonium acetate in refluxing butanol gave out the azadipyrromethene. Complexation of azadipyrromethene with an excess of trifluoride in dry DCM in the presence of DIPEA (base) at room temperature gave out an aza-BODIPY. To facilitate intersystem crossing, heavy atoms were introduced at the 2,6-positions, which was achieved by adding NBS or NIS at room temperature.

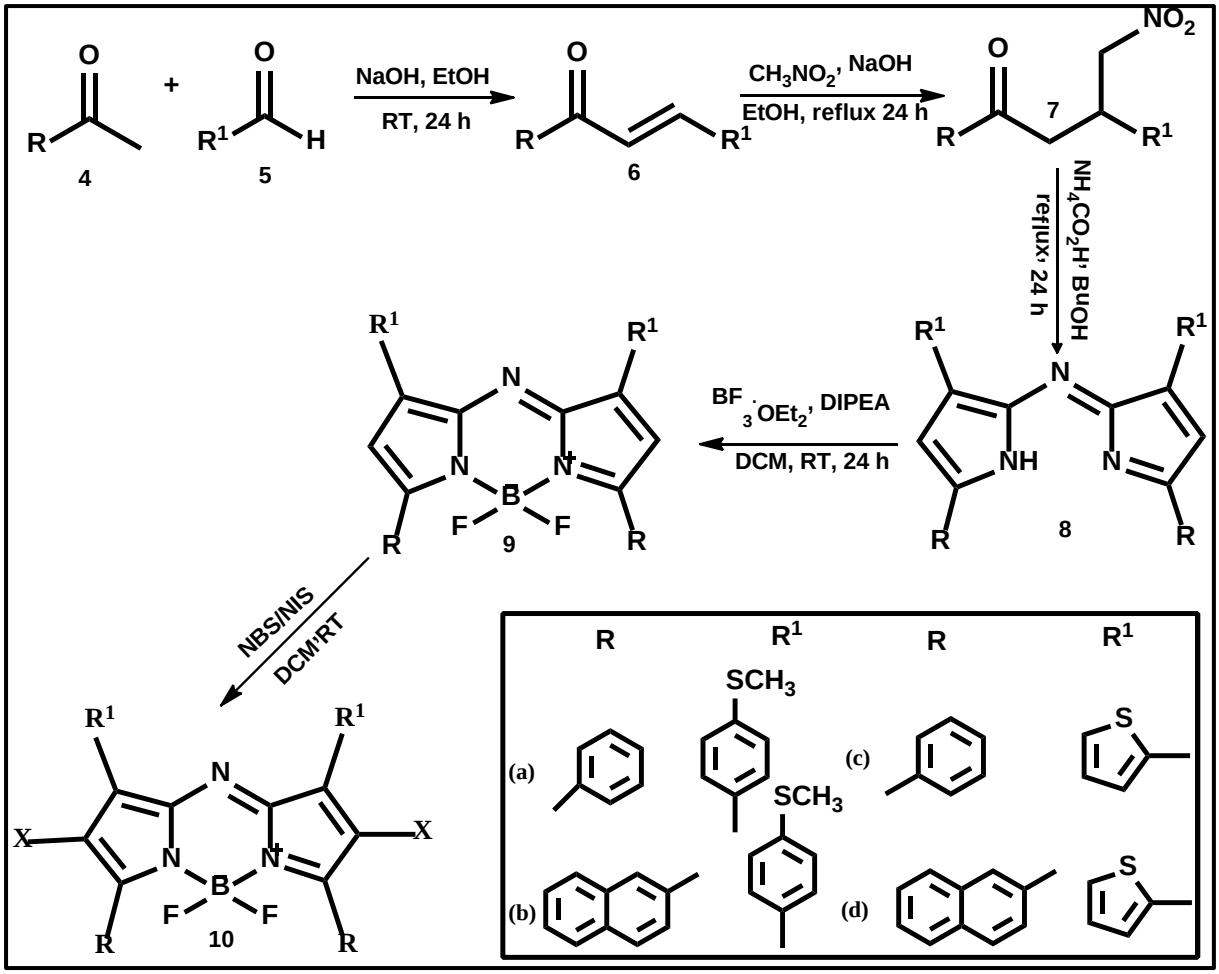

Scheme 3.1: A general synthetic pathway of halogenated aza-BODIPY. The inset provides the rings introduced at the 3,5- (R) and 1,7- (R^1) positions for the dyes labelled as **9a-d** and **10a-d**. The X at the 2,6-positions denotes a halogen atom.

3.1.2 Structural analysis

The ^{1}H NMR spectroscopy and MALDI-TOF-MS were used to confirm structures of synthesised aza-BODIPY. ^{1}H NMR was used to confirm the structure at hand with the spectrum observed by integrating the number of protons, and the MALDI-TOF-MS was used to confirm the molecular weight of the synthesised aza-BODIPY dyes.

For example, the twenty-five protons of Aza-BODIPY **10a** can readily be identified from the ^{1}H NMR spectrum (**Figure 3.1**). A singlet was observed at 2.81 ppm,

integrated into six protons attributed to the methylthiol, while the other nineteen protons lie in the aromatic region in the 7.3−8.3 ppm region. This includes the proton on the aza-BODIPY core in a similar manner to what has been reported previously for other aza-BODIPY dyes [94,95]. MALDI-TOF mass spectrometry confirmed that a parent peak was obtained for **10a** at 715.84 m/z, as shown in **Figure 3.2**.

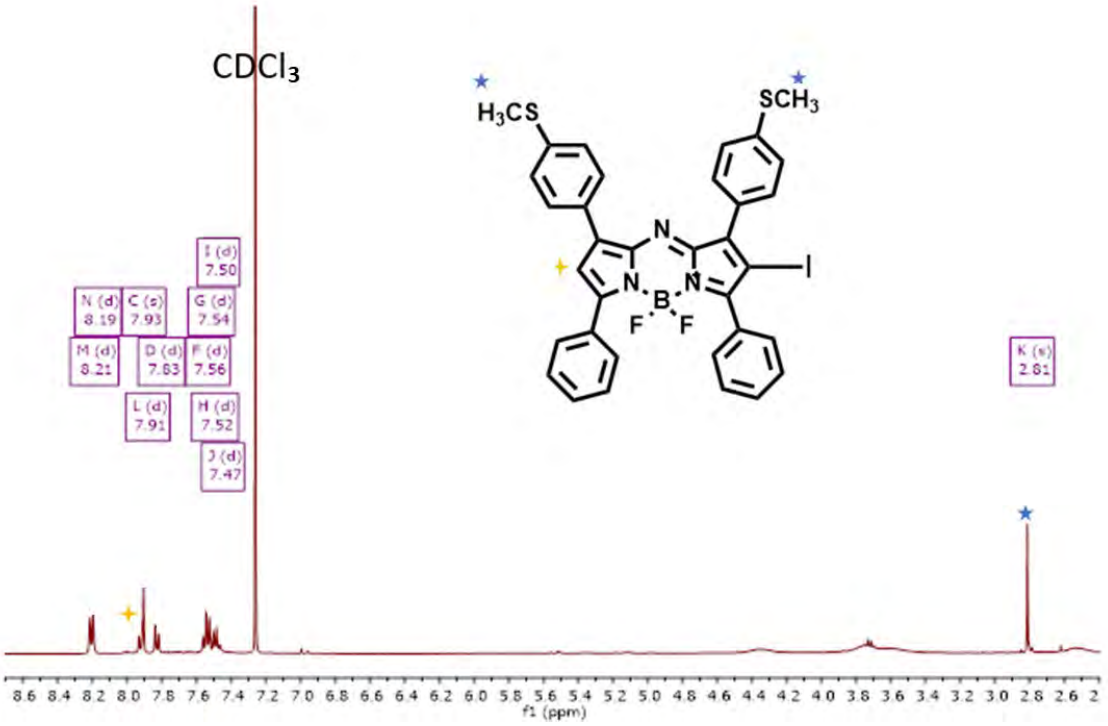

Figure 3.1: ^{1}H NMR spectrum of aza-BODIPY **10a** in $CDCl_3$. The blue stars highlight the six thiomethyl protons, while the yellow cross highlights the proton on the aza-BODIPY core.

^{1}H NMR peaks corresponding to the 18, 17, 29, 22 and 20 protons of **9c**, **9d**, **10b**, **10c** and **10d**, respectively, were assigned in a similar manner to those of **10a**. The anticipated parent peaks were readily identified by MALDI-TOF MS in each case (**Figure 3.3**).

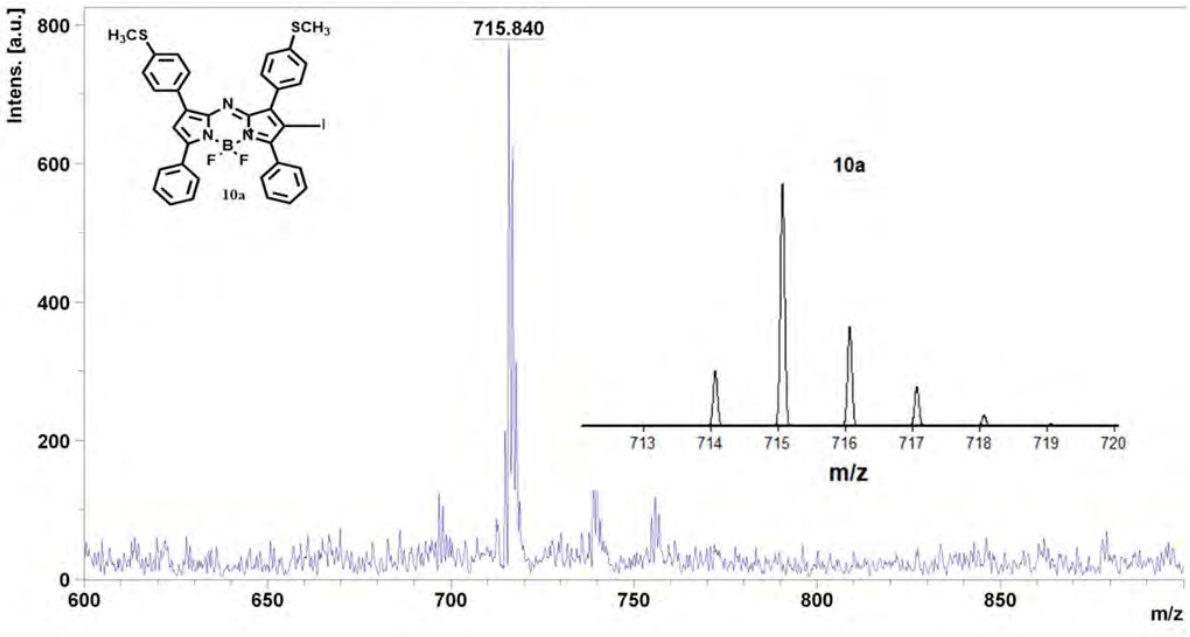

Figure 3.2: MALDI-TOF MS data for aza-BODIPY **10a**. Isotopic distributions were calculated with IsoPro 3.1 [96].

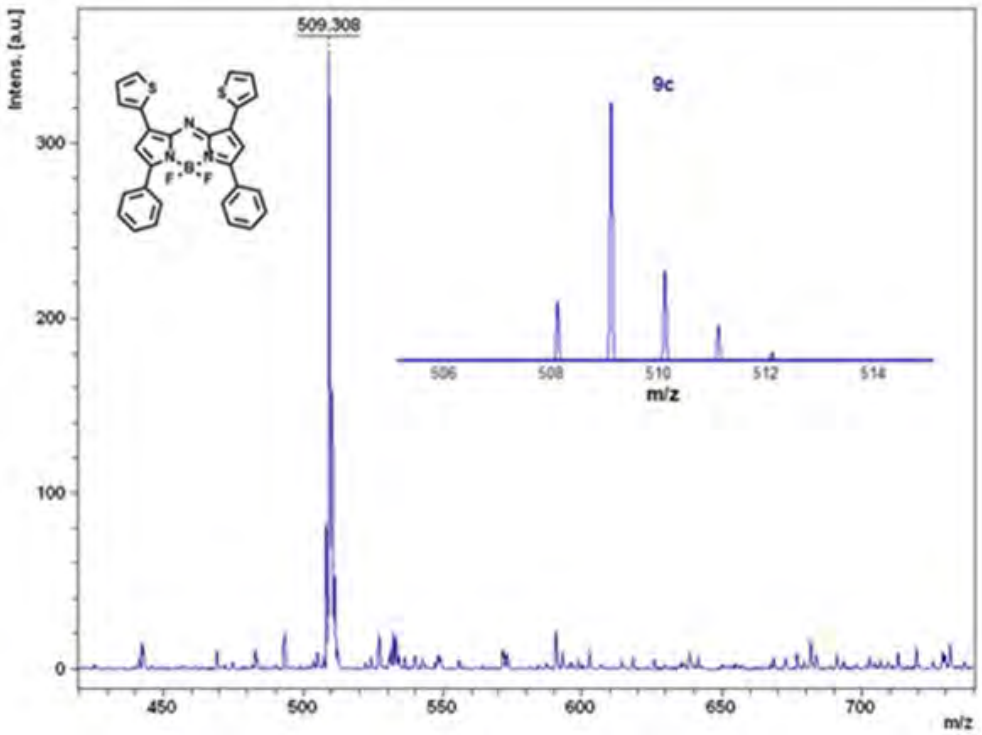

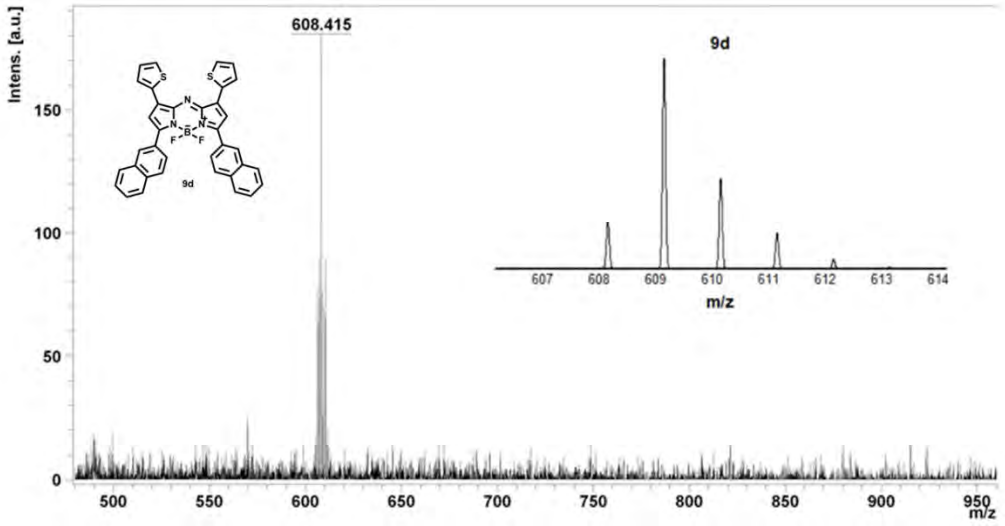
608.415
9d
Intens. [a.u.]
m/z

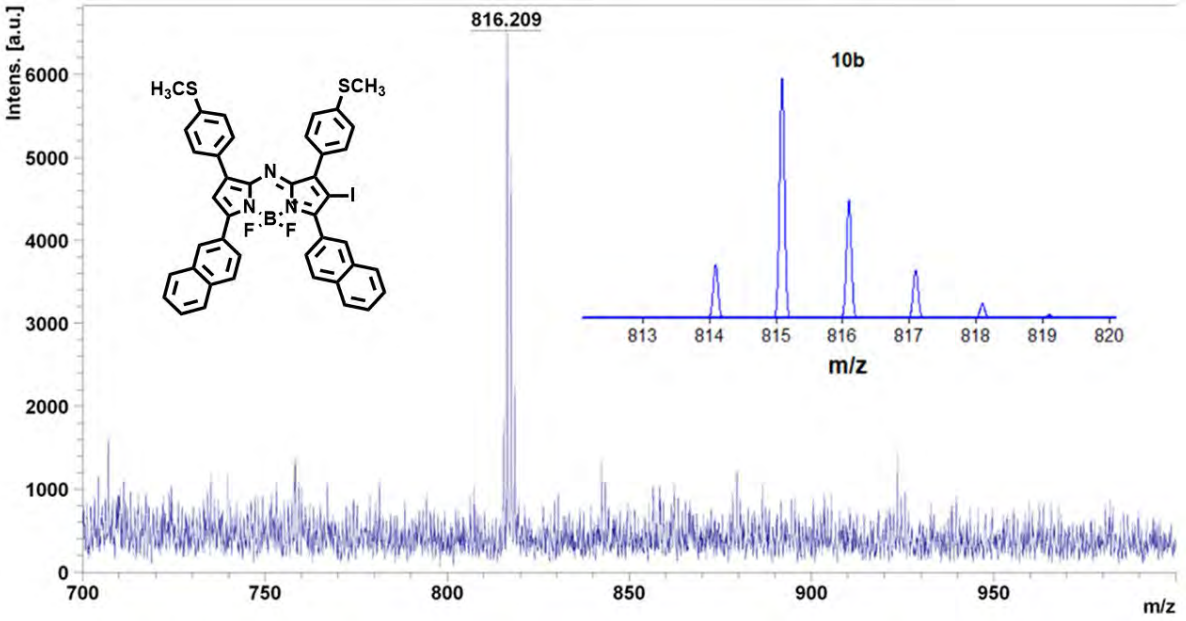
816.209
10b
H3CS
SCH3
Intens. [a.u.]
m/z

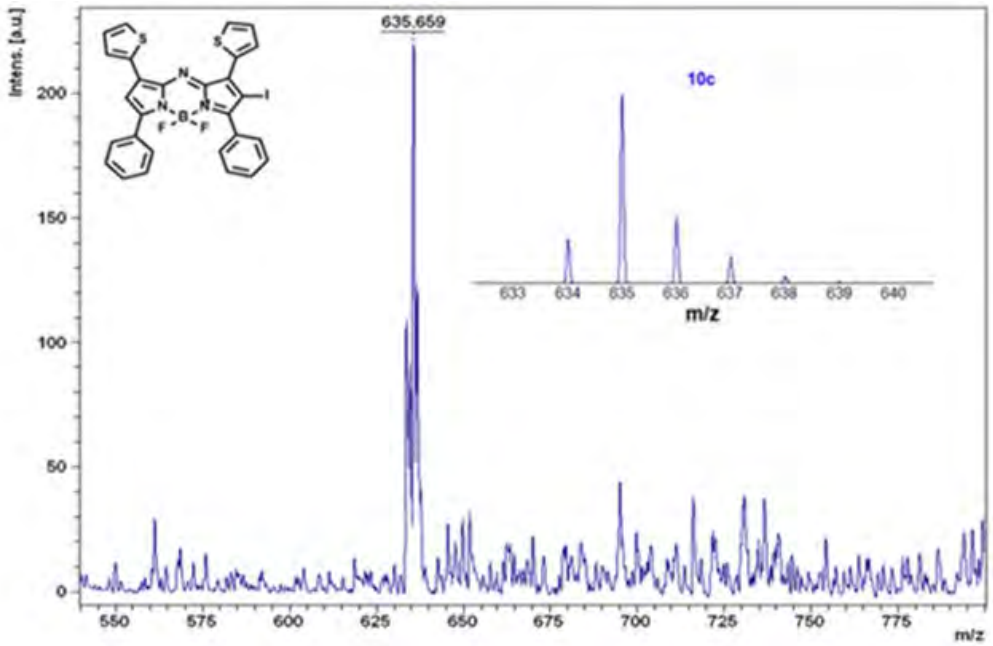
635.659
10c
Intens. [a.u.]
m/z

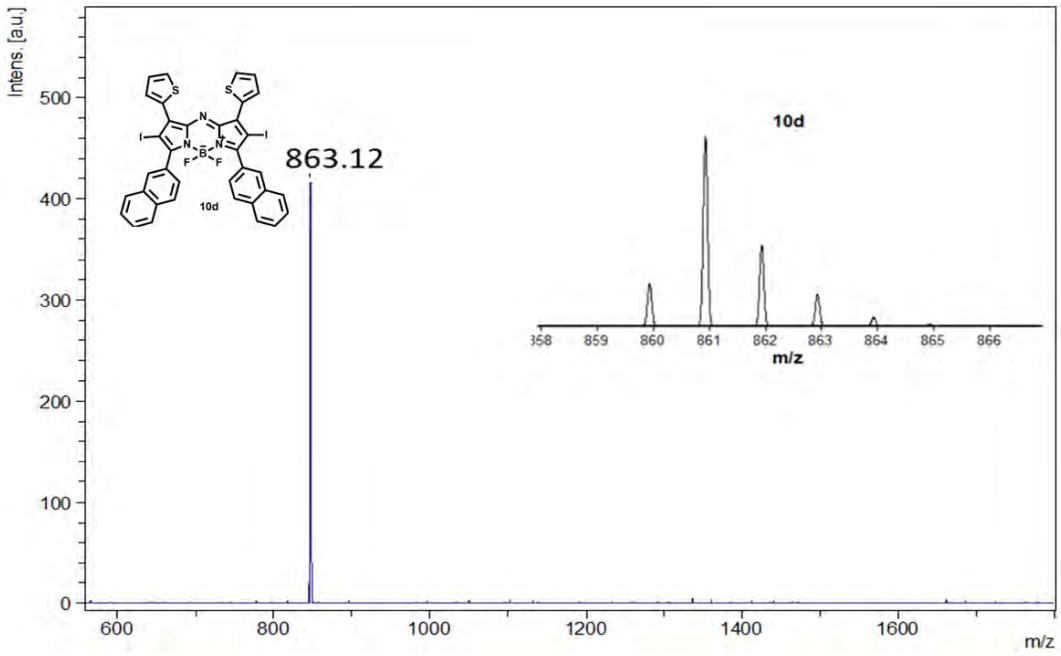

Figure 3.3: MALDI-TOF MS data for aza-BODIPYs **9c**, **9d**, **10b-d**. Isotopic distributions were calculated with IsoPro 3.1 [96].

3.1.3 Optical spectroscopy

The absorption spectra were used to identify the absorption band for all the dyes synthesised. The aza-BODIPY (**9c**, **9d**, and **10a-d**) dyes were studied in DMSO, as shown in **Figures 3.4** and **3.5**. The study compared the effect of incorporating the five-membered rings with having methylthiophenyl at the 1,7-positions. Aza-BODIPY **10a** and **10b** had methylthiophenyls at the β-position, and the phenyl or naphthyl rings at the α-position. Aza-BODIPY **9c** and **9d** were functionalised with thien-2-yl rings at the 1,7-positions and phenyl rings at the 3,5-positions. The difference is that **9c** has phenyl rings and **9d** has naphthyl rings. The absorption bands of **9d** and its iodinated analogue **10d** are more red shifted towards the NIR region than those of **9c** and **10c** (**Figure 3.4** and **Table 3.1**). Incorporating thien-2-yl rings to form **10a** and **10b** caused the main spectral bands to be more red-shifted than those of **10c** and **10d** (**Figures 3.4-3.5** and

Table 3.1). Upon adding heavy iodine atoms at the 2- and/or 6-positions to form **10c** and **10d**, a slight blue shift was observed relative to the spectra of **9c** and **9d** (**Figure 3.4** and **Table 3.1**), proving that halogenation was successful and that there was a narrowing of the HOMO−LUMO gap [53,95,97].

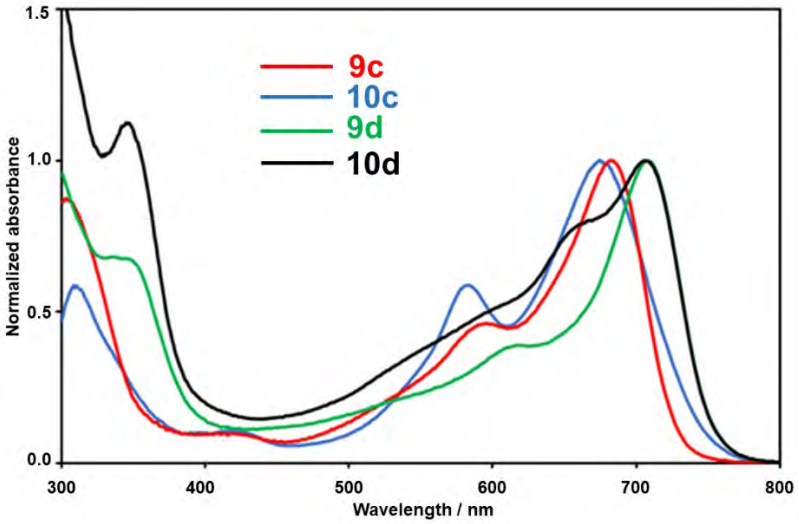

Figure 3.3: Normalised UV-visible absorption spectra of aza-BODIPY dyes **9c-d** and **10c-d** in DMSO.

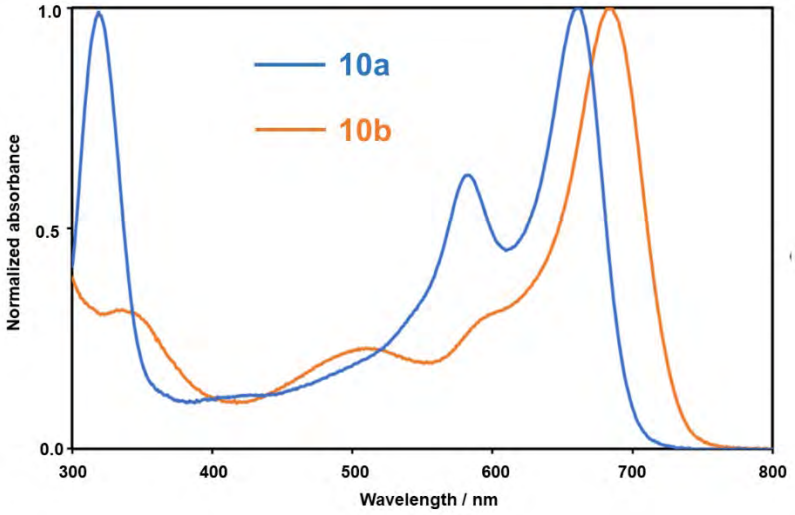

Figure 3.4: Normalised UV-visible absorption spectra of aza-BODIPYs **10a** and **10b** in DMSO.

3.2 Photophysicochemical studies of aza-BODIPY

3.2.1 Fluorescence studies

Diluted solutions of dye and standard (0.05−0.10 A) were used to measure the fluorescence properties. Fluorescence quantum yield measurements were carried out by using the comparative method using zinc phthalocyanines as standard. The compounds exhibited no fluorescence in either DMSO or DCM despite the fact that other aza-BODIPY dyes have been reported to exhibit moderately high fluorescence quantum yields [97]. Fluorescence emission consistent with triplet-triplet annihilation was sometimes observed at higher concentrations.

3.2.2 Singlet oxygen studies

Singlet oxygen quantum yields were obtained using the comparative methods with 1,3-diphenylisobenzofuran (DPBF) as the quencher and methylene blue as a standard with $\Phi_{\Delta} = 0.52$ in DMSO [88,98]. The singlet oxygen quantum yield was determined by the photodegradation of DPBF, as shown in **Figure 3.6**.

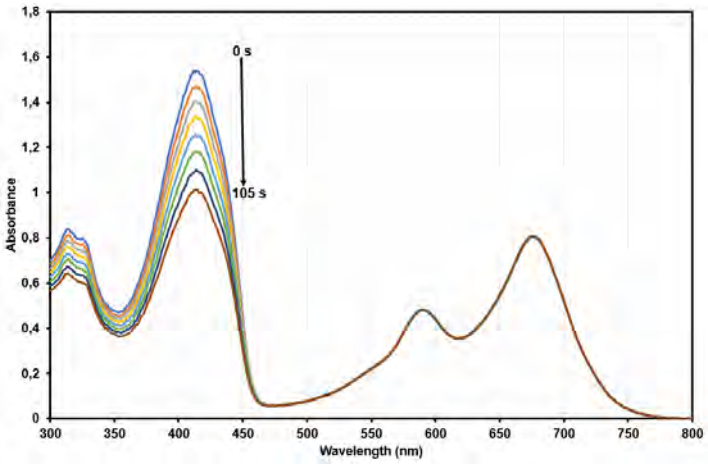

Figure 3.5: Singlet oxygen generation for **10c** monitored by the degradation of DPBF over 105 s at 15 s intervals in DMSO.

The photodegradation of DPBF was monitored through UV-visible absorption spectroscopy to determine the Φ_Δ values, as shown in **Figure 3.6**. Singlet oxygen quantum yields are an important parameter that can be used to assess the potential applicability of molecules for use as photosensitisers *via* the Type II mechanism during PDT. The DPBF degrades upon reacting with the singlet oxygen, as shown in **Figure 3.6**. The singlet oxygen quantum yields are quantified by plotting the change in absorbance of DPBF at 419 nm against the irradiation time by using methylene blue as a standard**.** A summary of the photophysicochemical parameters (Φ_F, Φ_Δ and τ_T) are summarised in **Table 3.1**. Triplet lifetimes were determined for the **9c**, **9d**, **10c** and **10d** series of dyes that were used for the PDT activity studies reported in Chapter 6 and ranged from 7.9−15 μs (**Table 3.1**). This enhances the suitability of the dyes as photosensitisers for biomedical applications such as PDT and PACT.

Table 3.1: Summary of the photophysicochemical properties of the aza-BODIPYs in DMSO.

	Absorbance (λ_{max})	**Φ_F**	**Φ_Δ**	**τ_T (μs)**
9c	682	0.01	0.23	12
9d	708	0.02	0.15	13
10a	663	0.001	0.82	--
10b	690	0.002	0.55	--
10c	677	< 0.01	0.78	15
10d	707	< 0.01	0.82	7.9

3.3 Concluding remarks

The synthesised aza-BODIPY dyes were characterised by ^{1}H NMR, UV-visible absorption spectroscopy, and mass spectrometry to confirm that the dyes were successfully synthesised. The main spectral bands in the UV-visible absorption spectra

of the dyes were more red shifted into the NIR region. The thien-2-yl rings resulted in a red-shift of the main spectral band compared to dyes with methylthiophenyl rings.

CHAPTER 4

SYNTHESIS AND CHARACTERISATION OF NANOCONJUGATES

This chapter describes the synthesis and characterisation of aza-BODIPYs conjugated to gold nanoparticles.

4. Conjugation of aza-BODIPY dye into AuNPs

4.1 Aza-BODIPY dyes and their nanoconjugates

Attempts were made to conjugate aza-BODIPY dyes **10a**, **10b**, **10c,** and **10d** (**Figure 4.1**) to AuNPs to enhance aqueous solubility and the photophysicochemical properties. Conjugation of **10c** and **10d** was unsuccessful, but **10a**-AuNPs and **10b**-AuNPs nanoconjugates were successfully prepared. This was confirmed using UV-visible absorption spectroscopy spectroscopy and a range of other techniques.

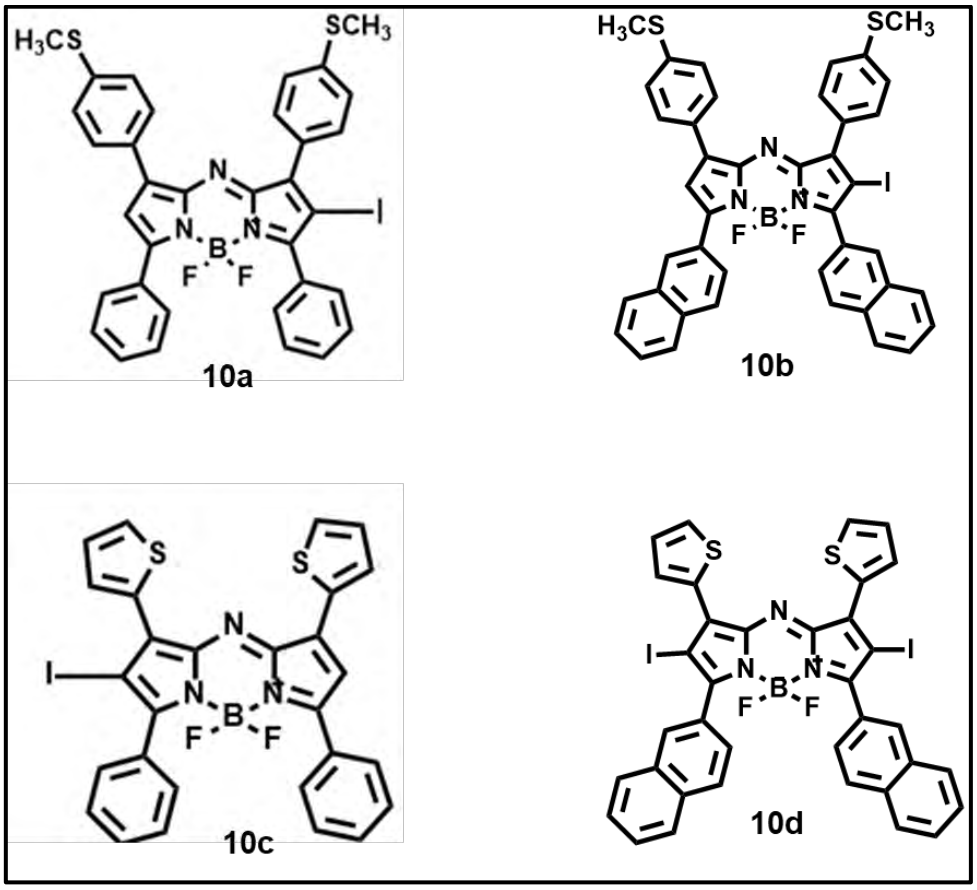

Figure 4.1: Aza-BODIPY used for conjugation with AuNPs.

4.2 Characterisation of aza-BODIPY-AuNPs

The characterisation techniques that were used to confirm the conjugation include Dynamic light scattering (DLS), Energy dispersive X-ray spectroscopy (EDS), Transmission electron microscopy (TEM), and X-ray diffraction (XRD).

4.2.1 UV-visible absorption spectroscopy

The UV-visible absorption spectroscopy spectra of **10a**-AuNPs and **10b**-AuNPs show the characteristics of the SPR band (**Figure 4.2**). The AuNPs absorb at λ_{max} 531 nm, **10a** at 663 nm, and **10b** at 690 nm. Upon conjugation, a hypsochromic shift was observed from the main spectral bands of the AuNPs and **10a**-AuNPs, whereby the AuNPs band was observed at 528 nm, and the main spectral band of conjugate **10a**-AuNPs was at 661 nm, and **10b**-AuNPs was at 688 nm.

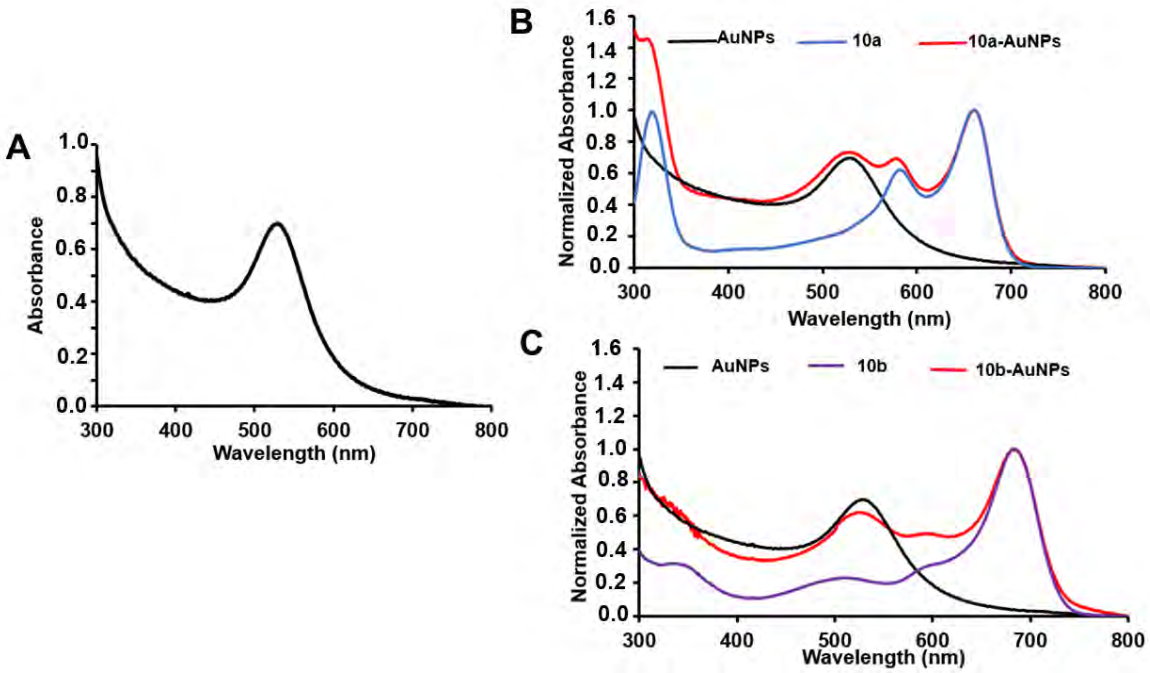

Figure 4.2: The UV-visible absorption spectra of A) AuNPs, B) AuNPs, **10a**, and **10a**-AuNPs, and C) AuNPs, **10b** and **10b**-AuNPs in DCM.

Table 4.1: Loading of conjugates determined by UV-visible absorption spectroscopy.

Complex/conjugate	Loading (µg/mg)
10a	–
10b	–
10a-AuNPs	0.75
10b-AuNPs	0.71

4.2.2 Transmission electron microscope (TEM) images

The TEM images of AuNPs and the nanoconjugates were obtained to evaluate the shape and estimate the size of AuNPs. The AuNPs alone were monodispersed with nanospheres ranging between 2−15 nm in size. However, upon conjugation, an increase in the size was observed, as shown in **Figure 4.3**.

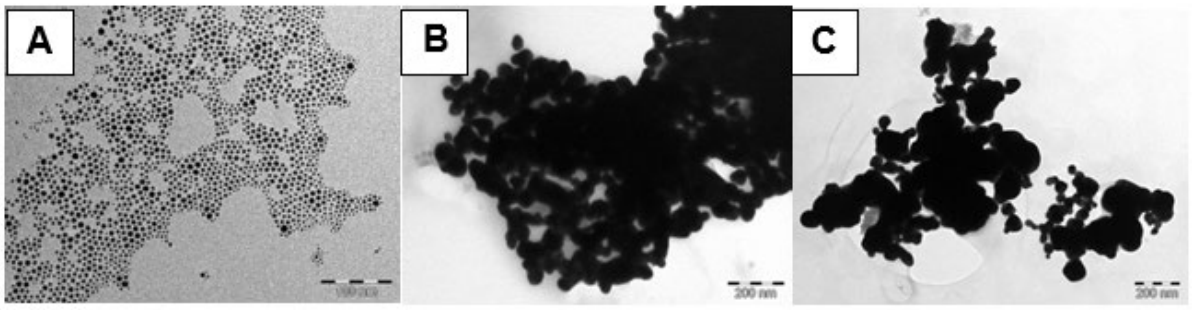

Figure 4.3: TEM images of (A) AuNPs, (B) **10a**-AuNPs and (C) **10b**-AuNPs in chloroform.

4.2.3 Dynamic Light Scattering (DLS)

DLS was used to determine the hydrodynamic diameter (D_h) of nanoparticles and their nanoconjugates (**Figure 4.4**). The sizes of AuNPs alone were determined to be 2.3 nm and the nanoconjugate **10a** to be 8.67 nm and **10b** to be 11.64 nm.

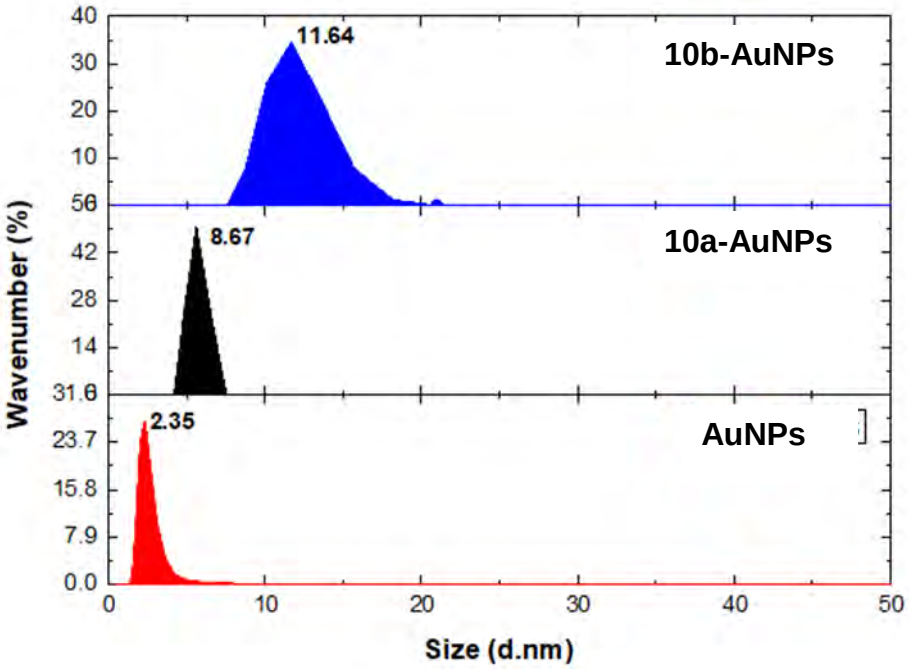

Figure 4.4: DLS curves for the AuNPs and the **10a**-AuNP and **10b**-AuNP nanoconjugates.

4.2.4 Energy-Dispersive X-ray Spectroscopy (EDS)

The spectra were used to qualitatively determine the elemental composition of AuNPs, and their conjugates, as shown in **Figure 4.5**. The EDS spectra of AuNPs show the presence of the expected metal element, which is Au. The EDS spectra of **10a** show the presence of C, N, B, F, S, I, while those of **10a**-AuNPs, and **10b**-AuNPs showed the presence of C, N, B, F, S, I, Au, which were the expected metal elements for the conjugate.

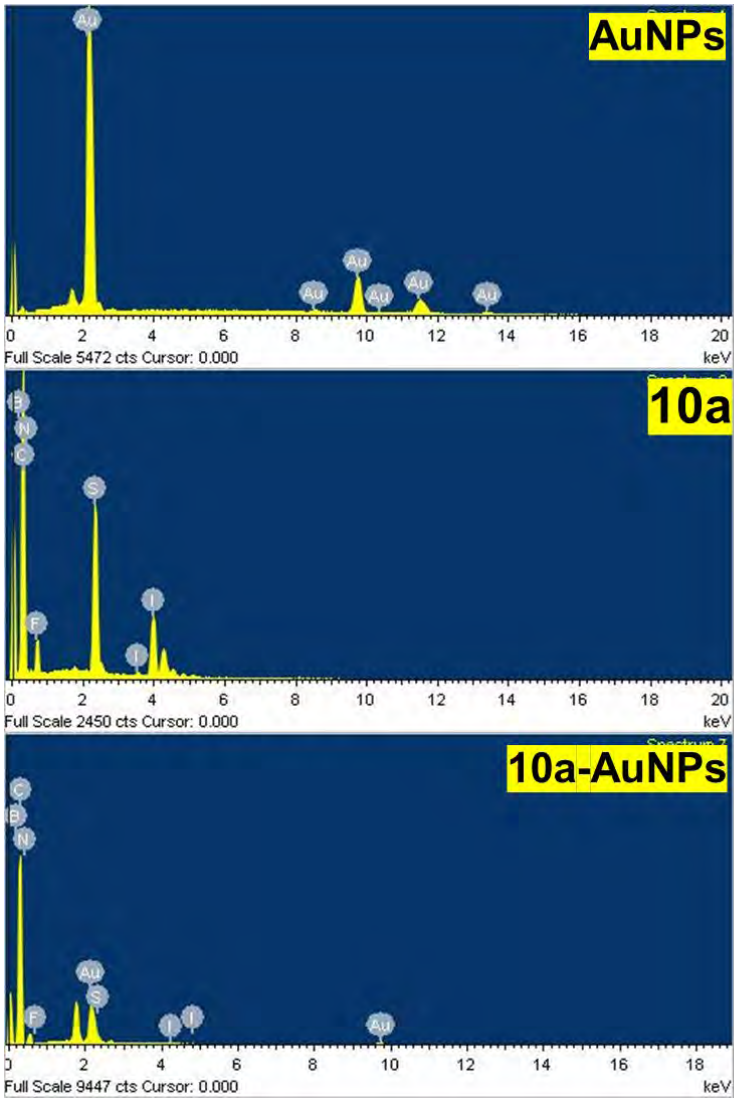

Figure 4.5: EDS spectra of (A) AuNPs, (B) **10a**-AuNPs, and (C) **10b**-AuNPs.

4.2.5 X-Ray Diffraction (XRD)

X-ray diffraction was used to determine the crystallinity of the compounds. In **Figure 4.6**, the XRD diffractogram for AuNPs, complex and conjugate show peak characteristics of AuNPs. There is complete crystallinity at 111, 200, 220, 311, and 222, with 2θ= 38.1, 44.3, 64.5, 77.7, and 81.9° planes of the face-centred-cubic structures of metallic gold [99]. XRD diffractograms for aza-BODIPY **10a** showed both amorphous and crystalline characteristics. It is predominantly amorphous. XRD diffractograms for

10a-AuNPs maintained the crystallinity, and amorphous characters imparted by the dye can still be observed around 2θ = 20°, confirming the conjugation.

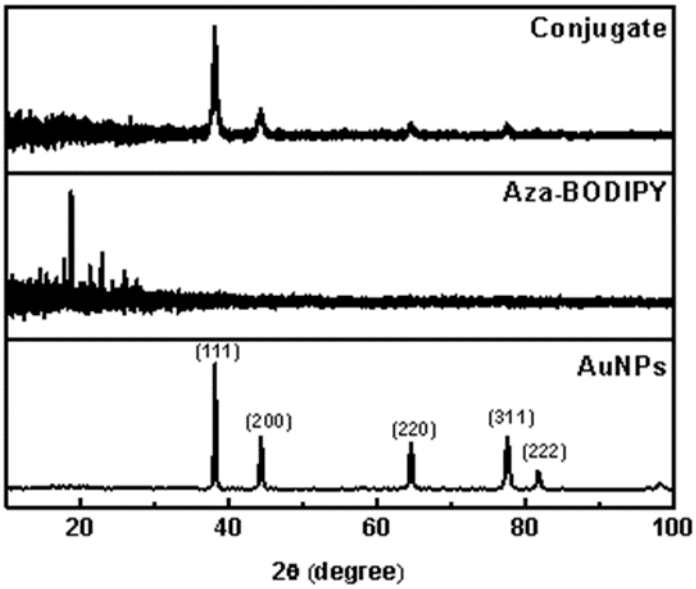

Figure 4.6: A typical example of the XRD pattern of AuNPs, **10a,** and **10a**-AuNPs.

4.3 Concluding remarks

The aza-BODIPY dyes and AuNPs were successfully synthesised and characterised using UV-visible absorption spectroscopy, DLS, TEM, and XRD. The conjugation of aza-BODIPY with AuNPs enhanced the singlet oxygen quantum yield, which resulted in enhanced PACT activity, as discussed further in Chapter 5.

CHAPTER 5

PHOTODYNAMIC ANTIMICROBIAL ACTIVITY STUDIES

This chapter discusses the photodynamic antimicrobial chemotherapy activity of aza-BODIPY dyes against *Staphylococcus aureus* and *Escherichia coli*.

5. Photodynamic Antimicrobial Chemotherapy

This chapter discusses the result obtained for PACT using aza-BODIPY dyes (**9c**, **9d, 10a**-**10d**) and their nanoconjugates (**10a**-AuNPs and **10b**-AuNPs) against *S. aureus*.

5.1 PACT studies of Staphylococcus aureus in solution

Photodynamic antimicrobial studies were performed in 1% DMSO since aza-BODIPY dyes are insoluble in PBS, but 1% DMSO enhanced the solubility. Concentrations of 5 µM for (**10a**, **10b**, **10a**-AuNPs and **10b**-AuNPs) at 90 min, and 10 µM for (**9c**, **9d**, **10c**, and **10d**) at 60 min were selected after an initial study of log reduction against concentration after a fixed irradiation time of 60 min. Minimal log reduction values were obtained against *E. coli* in this context, so the full time-dependent PACT studies were only carried out against *S. aureus*.

To define 100% bacteria colony survival, the zero irradiation time was used, as shown in **Figure 5.1**. Dark toxicity studies demonstrated that treatment with the aza-BODIPY had limited antibacterial effects (**Figures 5.1**−**5.3**). This study explored the antimicrobial activity of aza-BODIPYs **10a** and **10b** and their nanoconjugates using PACT by irradiating at 660 nm and a concentration of 5 µM. The nanoconjugates performed better against *S. aureus* with 9.41 log reduction and 0.00% cell survival showing that AuNPs influenced the photoinactivation (**Table 5.1**). Aza-BODIPYs **9c** and **9d** did not perform well due to their relatively low Φ_Δ values. Aza-BODIPYs **10c** and **10d** performed better with log a reduction of 8.94, since they are iodinated, showing the effect of incorporating heavy atoms and the resulting higher Φ_Δ values.

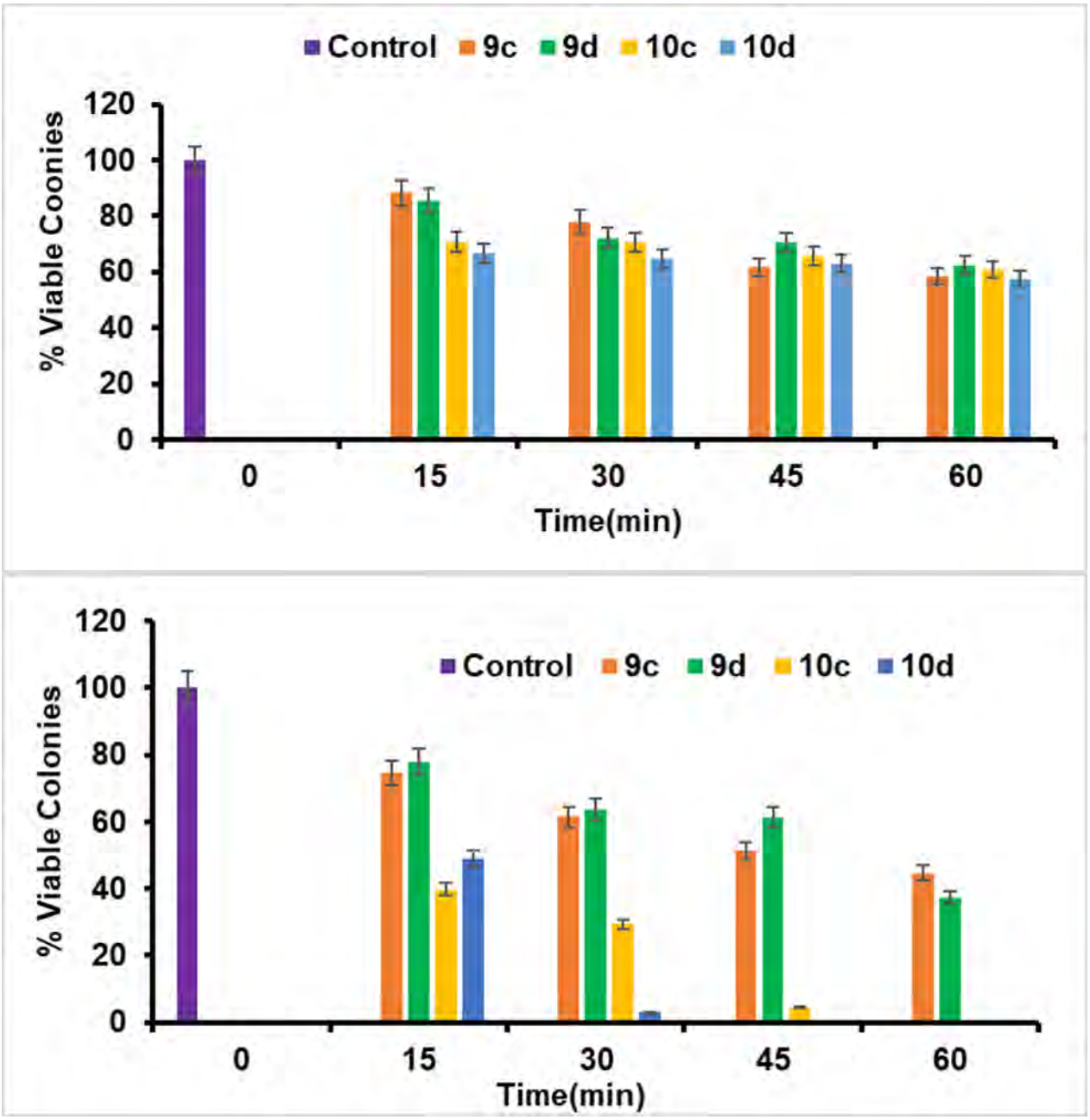

Figure 5.1: The dark toxicity (TOP) and upon irradiation (BOTTOM) studies conducted against *S. aureus* in 1% DMSO/PBS. Measurements were made in triplicate. The error bars refer to the standard deviation.

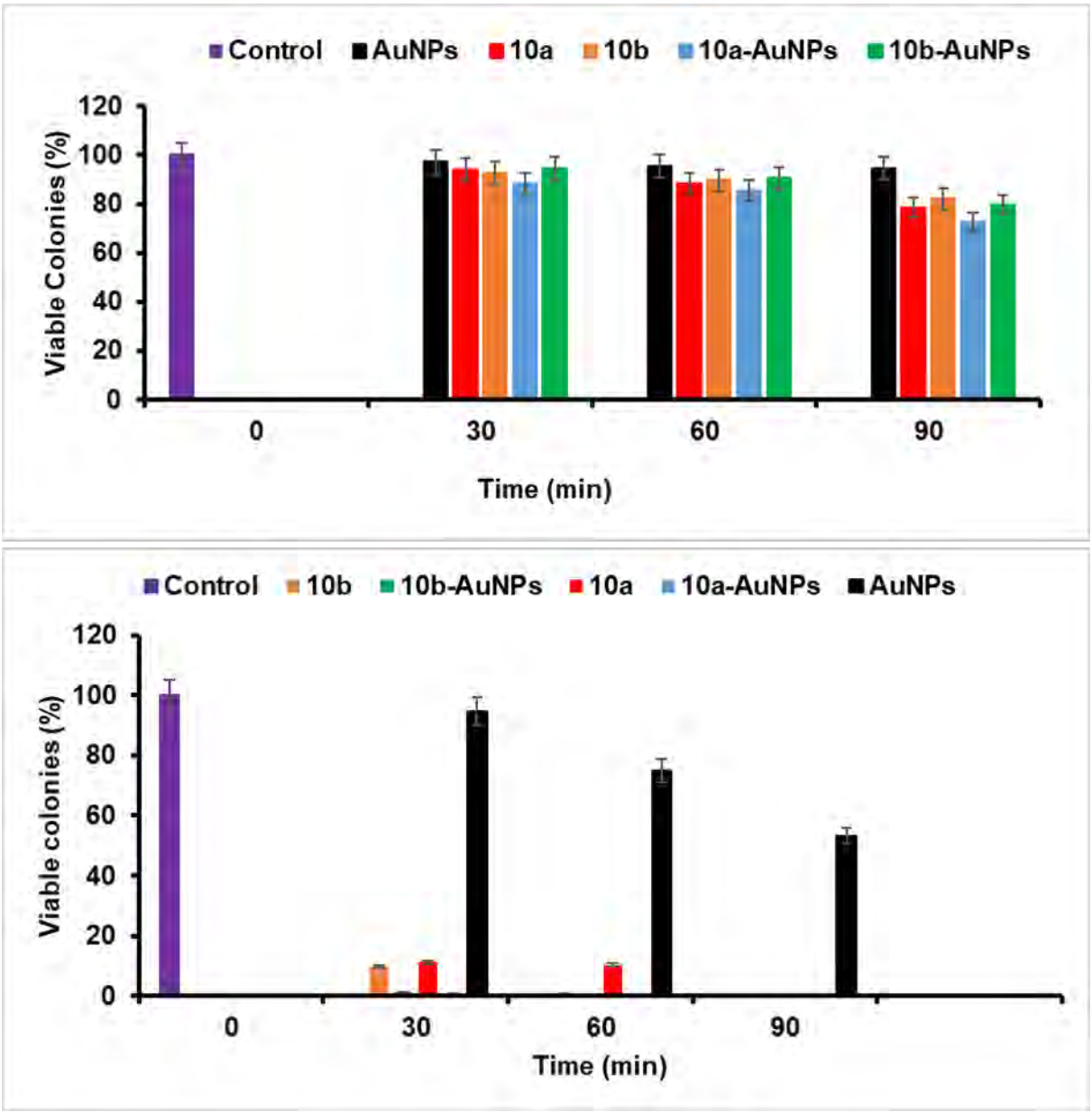

Figure 5.2: The dark toxicity (TOP) and upon irradiation (BOTTOM) studies conducted against *S. aureus* in 1% DMSO/PBS. Measurements were made in triplicate. The error bars refer to the standard deviation.

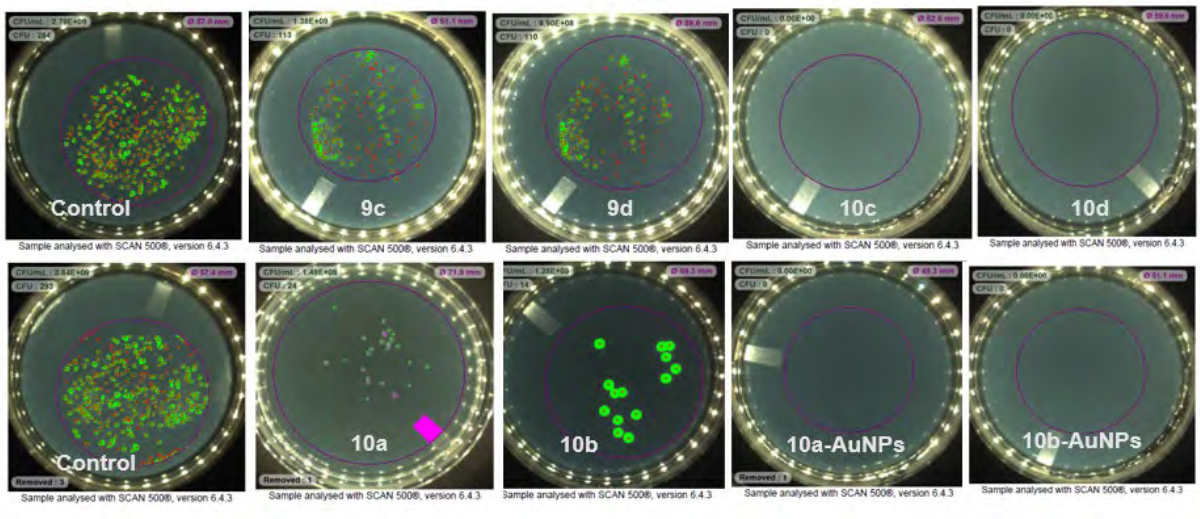

Figure 5.3: Agar plates of *S. aureus* upon 60 min irradiation with 660 and 730 nm Thorlabs LED.

Table 5.1: Log reduction values for the photoinactivation effect against *S. aureus* of **9c**, **9d**, **10c** and **10d** (5 µM at 60 min irradiation), and of **10a**, **10b**, **10a**-AuNPs and **10b**-AuNPs (5 µM at 90 min irradiation) in 1% DMSO/PBS.

	Log reduction
9c	0.35
9d	0.43
10a	8.94
10a-AuNPs	9.41
10b	8.94
10b-AuNPs	9.41
10c	8.94
10d	8.94

5.2 Concluding remarks

The PACT activities of aza-BODIPY dyes **9c-d**, **10a-d** and the **10a**-AuNP and **10b**-AuNP nanoconjugates were evaluated against *S. aureus* and *E. coli*. The data obtained were analysed by using log reduction value, which shows that the conjugated aza-

BODIPY dyes had the greatest value of 9.41, while the iodinated dyes had a log reduction of 8.94, while non-iodinated aza-BODIPYs **9c** and **9d** had exceptionally low log reduction values of 0.35 and 0.43, respectively. It can be concluded that nanoconjugation with AuNPs and the introduction of iodine heavy atoms influences the photoinactivation against *S. aureus.* In an earlier PACT activity study against *S. aureus* by Dubazana that also used Thorlabs LEDs in a similar manner [63] with two dibrominated tetraphenyl-substituted aza-BODIPY dyes log reduction values of *ca.* 1.0 were obtained, so the structural modifications made in this study significantly enhanced the PACT activities.

CHAPTER 6

IN VITRO PHOTODYNAMIC THERAPY ACTIVITY OF AZA-BODIPY DYES

This chapter discusses the *in vitro* dark cytotoxicity and photodynamic therapy activity of aza-BODIPY dyes against MCF-7 breast cancer cells.

6. Photodynamic Therapy

In vitro studies were carried out against MCF-7 cancer cells. The MTT assay was used to determine the percentage of viable cells [100]. Photodynamic activity (light) and dark toxicity were investigated for aza-BODIPY dyes (**9c**, **9d**, **10c,** and **10d**). This was evaluated by calculating the half-maximal inhibitory concentration (IC_{50}) value. The IC_{50} values were used to characterise the effectiveness of the dyes in inhibiting a specific biological or biochemical function.

6.1 *In vitro* studies in photodynamic activity and dark toxicity of aza-BODIPYs (9c, 9d, 10c, and 10d).

6.1.1 Photodynamic effect

In vitro, photodynamic activity properties of aza-BODIPY (**9c**, **9d**, **10c,** and **10d**) were conducted using an MTT assay on MCF-7 cancer cells following the procedure reported previously in the literature [100]. These studies were conducted over a concentration range of 0−50 µM. The aza-BODIPY (**9c**, **9d**, **10c,** and **10d**) were illuminated in 96 well plates for 20 min using Modulight® Medical 7710-680 Laser fitted with a Thorlabs M660L4 660 nm LED with irradiance values of 280 $mW.cm^{-2}$. These studies were conducted in 1% DMSO due to the insolubility of compounds in an aqueous solution. The cell viabilities are shown in line graphs, **Figure 6.1** showing dark toxicity and light studies. No cytocidal effects were observed on the MCF-7 cells in the absence of the aza-BODIPY dyes. Minimal dark toxicity was observed for all the complexes at low concentrations, as shown in **Figure 6.1**, but a slight decrease was observed with increasing concentration.

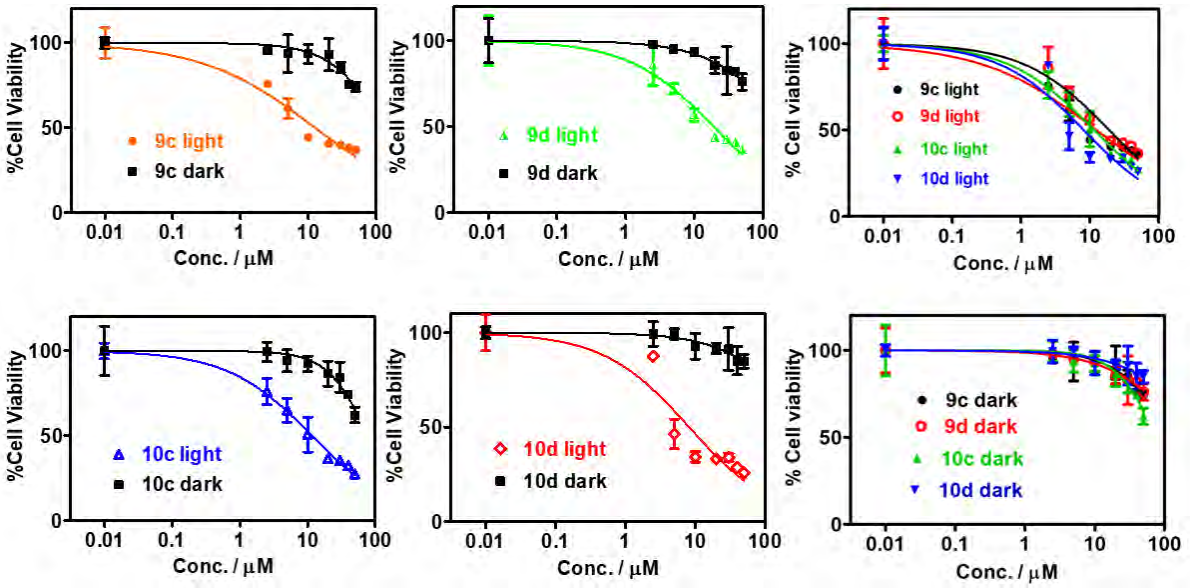

Figure 6.1: Cytotoxicity of aza-BODIPY dyes **9c**, **9d**, **10c,** and **10d** against MCF-7 cells after 24 h incubation in the dark and after irradiation (light). Measurements were made in triplicate. The error bars refer to the standard deviation.

Table 6.1: Summary of the Φ_Δ values for the dyes in DMSO, percentage cell viability at 50 µM, and IC_{50} values for all compounds against MCF-7 breast cancer cells *in vitro*.

	Φ_Δ	**Cell viability (%)**	**IC_{50} (light)** µM	**IC_{50} (dark)** µM
9c	0.23	30.4	12.5	> 50
9d	0.15	36.8	19.2	> 50
10c	0.78	26.2	11.6	> 50
10d	0.82	27.6	8.2	> 50

The trends in the Φ_Δ and PDT activity values (**Table 6.1**) for the non-iodinated and iodinated compounds is that for **10c** and **10d**, there is a decrease in the IC_{50} values and hence an increase in the PDT activity relative to **9c** and **9d**. The iodinated **10c** and **10d** dyes exhibit higher PDT activity than the non-iodinated **9c** and **9d** dyes due to their higher singlet oxygen quantum yields.

6.2 Cellular Uptake

The cellular uptake of compounds **9c**, **9d**, **10c**, and **10d** were determined to estimate the amount of dye available in cells for PDT after 24 h incubation. The cellular of non-iodinated and iodinated compounds was obtained to evaluate the effect of heavy atoms on the uptake. The cellular uptake curves of all the complexes are shown in **Figure 6.2**, demonstrating that the cellular uptake increases with concentration. The maximum uptake concentrations for complexes **9c**, **9d**, **10c,** and **10d** were greater than 50 µM, meaning if the concentration were increased to 100 µM or higher, a plateau or decline may have been noticed.

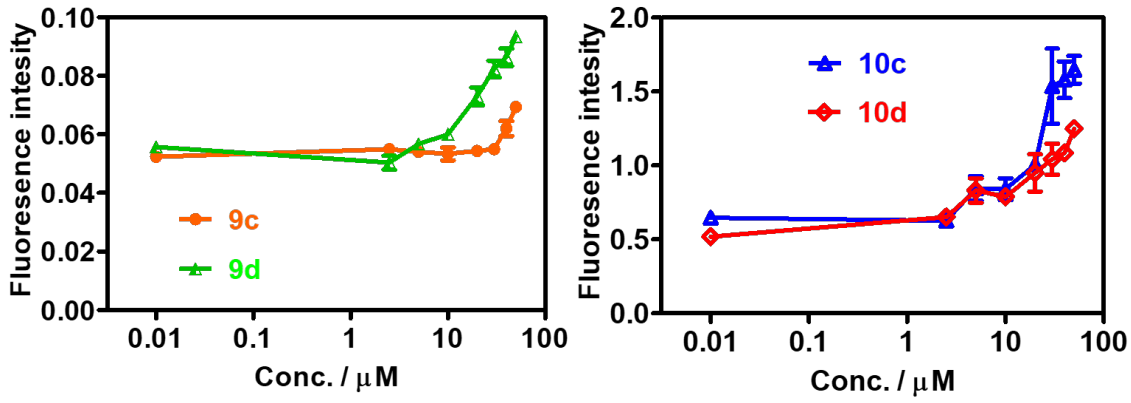

Figure 6.2: MCF-7 cellular uptake over 24 h for (**a**) **9c** and **9d** and (**b**) **10c** and **10d** as determined by fluorescence intensity using an ELISA reader with excitation and emission wavelengths of 660 and 680 nm. Measurements were made in triplicate. The error bars refer to the standard deviation.

6.3 Cell Imaging

The cell imaging under a microscope provided in **Figure 6.3** shows the effect of aza-BODIPY PS dyes **9c**, **9d**, **10c**, and **10d** on the MCF-7 cells before and after 20 min

irradiation with the PS dye treated MCF-7 cells exhibiting cell shrinkage and decreased cell density compared to the non-irradiated control cells in a manner that is consistent with the apoptotic process [101].

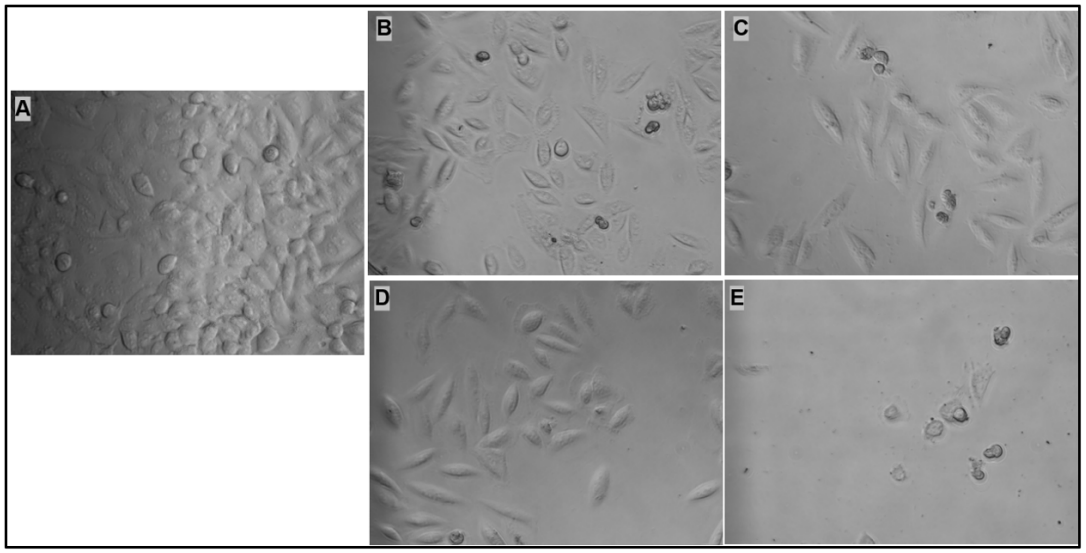

Figure 6.3: Microscopy images of the MCF-7 cells on clear-bottom 96-well plates in 1% DMSO-cultured media inoculated with 50 µM of (**9c**, **9d**, **10c,** and **10d**) incubated at 37 ºC at 5% CO_2, **A**) the control cells, **B**) **9c** after 20 min irradiation, C) **9d** after 20 min irradiation, **D**) **10c** after 20 min irradiation, **E**) **10d** after 20 min irradiation. Scale bar: 200 µm.

6.4 Concluding remark

The IC_{50} values obtained are comparable to those reported in an earlier PDT activity study against *MCF-7* breast cancer cells by Dubazana that also used Thorlabs LEDs in a similar manner [63] with two dibrominated tetraphenyl-substituted aza-BODIPY dyes. Although the PDT activity of iodinated compounds **10c** and **10d** is higher when compared to those of non-iodinated compounds **9c** and **9d**, the difference in the IC_{50} values is smaller than would be anticipated based on the large difference in the Φ_{Δ}

values. This merits further in-depth investigation and may be related to differences in lipophilicity of the PS dyes. Further modification of the aza-BODIPYs to enhance their aqueous solubility may be necessary. This topic will be discussed in more detail in Chapter 8. The study has shown that dark toxicity had minimal effects on all compounds, since IC_{50} > 50 μM in each case. Time constraints and issues encountered when growing the necessary MCF-7 cells made it impossible to carry out PDT activity studies on **10a**, **10b**, **10a**-AuNPs and **10b**-AuNPs, but this will be done in the near future.

CHAPTER 7

MOLECULAR MODELLING

This chapter analyses trends in UV-visible absorption spectra and electronic structures of the aza-BODIPY dyes.

7. Molecular Modelling

7.1 Geometry Optimization and TD-DFT calculations

Molecular modelling has been used to predict trends in the predicted spectra and electronic structures of the synthesised aza-BODIPY dyes. Density functional theory (DFT) was used to predict the photophysical properties of these dyes. The Gaussian 09 software package [102] was used to perform geometry optimisation calculations using the Beck, three-parameter, Lee-Yang-Parr (B3LYP) functional with SDD basis set. SDD basis sets were used since they provide a reasonable approximation for all atoms, including heavy atoms, such as iodine or bromine, used in this study. The B3LYP functional was adopted for structural analysis. The electronic absorption properties were calculated by time-dependent method (TD-DFT) using the Coulomb-attenuated B3LYP (CAM-B3LYP) functional with SDD basis set, which contains a long-range correction of the exchange potential. It is achieved by combining the elements of the hybrid B3LYP with increasing fractions of Hartree-Fock (HF) exchange as the interelectronic separation increases [103,104].

7.2 Molecular modelling for aza-BODIPY (9c-d and 10a-d)

This section explores trends in the electronic absorption spectra of aza-BODIPY dyes **9c-d** and **10a-d**, and model complexes consisting of an unsubstituted aza-BODIPY core (**core**) and a 1,3,5,7-tetraphenyl-aza-BODIPY (**4ph**). Complexation by BF_2 results in the HOMO and LUMO being well separated in terms of energy from the other MOs (**Figure 7.1**). As would normally be anticipated on this basis [41], the TD-DFT calculations predict that the HOMO → LUMO one-electron transition provides the

dominant contribution to the main absorption band in each case (**Table 7.1**). When considering how the structural changes modify the properties of the main spectral band, only the HOMO and LUMO hence need to be considered. The structural modifications cause a red shift of the main aza-BODIPY spectral band due to a narrowing of the HOMO−LUMO energy gap.

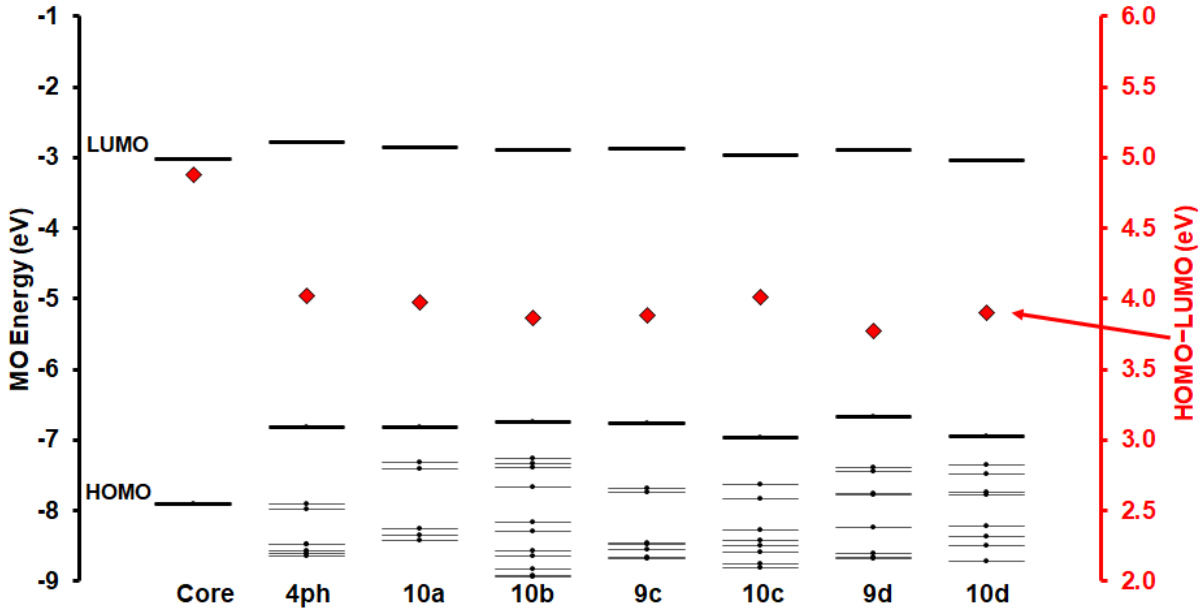

Figure 7.1: Frontier MO energies and HOMO–LUMO gaps of the aza-BODIPY dyes at the CAM-B3LYP/SDD level of theory. The HOMO and LUMO are highlighted with darker lines. The red diamonds denote the HOMO–LUMO band gaps and are plotted against the secondary axis. Small black circles highlight occupied MOs.

In contrast with BODIPY dyes [41], the introduction of the aza-nitrogen atom at the bridging position results in a stabilisation of the LUMO since there is a large MO coefficient at this position (**Figure 7.2**) and this results in a large red shift of the main spectral band. Introduction of the aryl groups of the **4ph** model complex, and **9c-d** and **10a-d** results in a large red shift of the main spectral band since there are large MO

coefficients in the HOMO at the 1,3,5,7-positions (**Figure 7.2**). The introduction of electron-rich aryl rings narrows the HOMO−LUMO gap due to the mesomeric interactions with the aza-BODIPY core. The TD-DFT calculations of the aza-BODIPY dyes (**Table 7.1**) demonstrate that adding aryl rings at the α-positions has more effect on the MO energies than is the case at the β-positions, since a greater red-shift is observed for the dyes that have naphthyl rather than phenyl rings at these positions (**Table 7.1** and **Figure 7.3**). The HOMO has larger MO coefficients at these positions (**Figure 7.2**) so the introduction of a more electron rich group at this position results in a relative destabilisation of this MO and a further narrowing of the HOMO−LUMO gap.

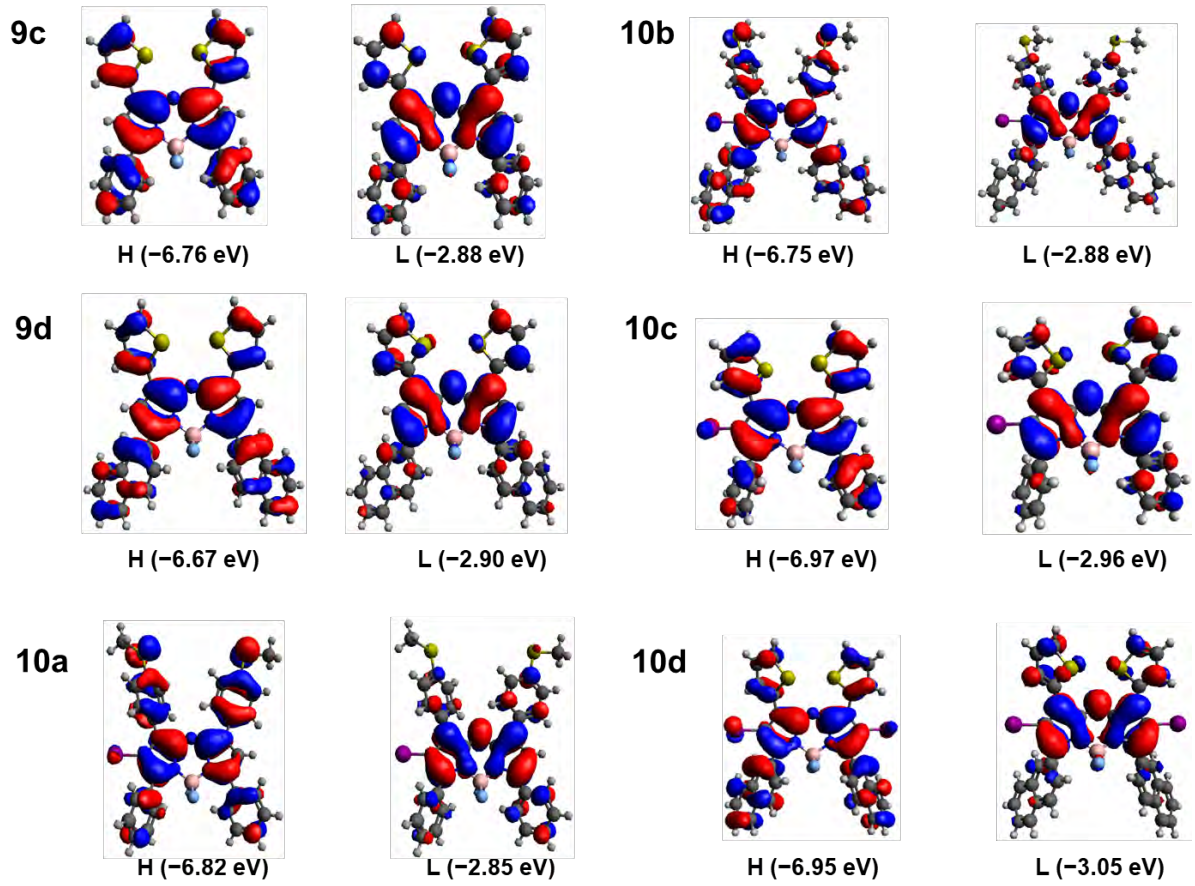

Figure 7.2: Angular nodal patterns at an isosurface value of 0.02 a.u. and MO energies of the HOMO and LUMO of aza-BODIPY dyes **9c-9d** and **10a-10d** at the CAM-B3LYP/SDD level of theory. H and L = HOMO and LUMO, respectively.

When the Ph-SMe substituted compounds (**10a-b**) are compared to those containing thien-2-yl rings (**10c-d**) shows that the introduction of thien-2-yl rings cause a destabilisation of the HOMO energy and a narrower HOMO−LUMO gap (**Figure 7.2**), which is consistent with the experimentally observed red shift of the main spectral bands of **10c** and **10d**. Surprisingly this trend is not predicted in the calculated TD-DFT spectra (**Figure 7.3**). The effect of incorporating heavy atoms in the context of **10c** and **10d**, results in a stabilisation of the HOMO and LUMO relative to those of **9c** and **9d**. There is a relative stabilisation of the HOMO, which increases the HOMO−LUMO energy

gap resulting in an observed blue shift in the main spectral band of **10c** (**Table 7.1** and **Figure 7.3**). In the context of **10d**, the introduction of a second results in a significantly smaller blue shift possibly due to the additional mesomeric interactions between the lone pairs on the iodine atoms and the aza-BODIPY core.

Table 7.1: Calculated and observed electronic excitation spectra of aza-BODIPY dyes (**core**, **4Ph**, **9c-9d**, and **10a-10d**) based on TD-DFT calculations using the B3LYP functional with SDD basis sets.

	#[a]	E[b] (eV)	f[c]	λ_{calc}[d] (nm)	λ_{exp}[e] (nm)	ν[f] (cm^{-1})	Wavefunction =[g]
Core	1	2.88	0.42	431	---	23.2	99% H→L
4Ph	1	2.24	0.80	553	---	18.1	99% H→L
9c	1	2.19	0.59	565	682	17.7	98% H→L
9d	1	2.12	0.61	585	708	17.1	97% H→L
10a	1	2.22	0.79	557	663	18.0	97% H→L
10b	1	2.15	0.84	576	690	17.4	96% H→L
10c	1	2.19	0.78	567	677	17.6	98% H→L
10d	1	2.15	0.88	577	707	17.3	94% H→L

[a] – Number of the excited state in ascending energy. [b] – Calculated band energies reported in eV. [c] – Theoretically calculated oscillator strengths. [d] – Theoretically calculated wavelengths in nm. [e] – Experimental wavelengths obtained in DMSO and recorded in nm. [f] – Calculated band energies (10^3 cm^{-1}). [g] – Wavefunctions based on the eigenvectors predicted by TD-DFT calculation for the B3LYP geometries optimised using 6-31G(d) basis sets. H and L = HOMO and LUMO, respectively.

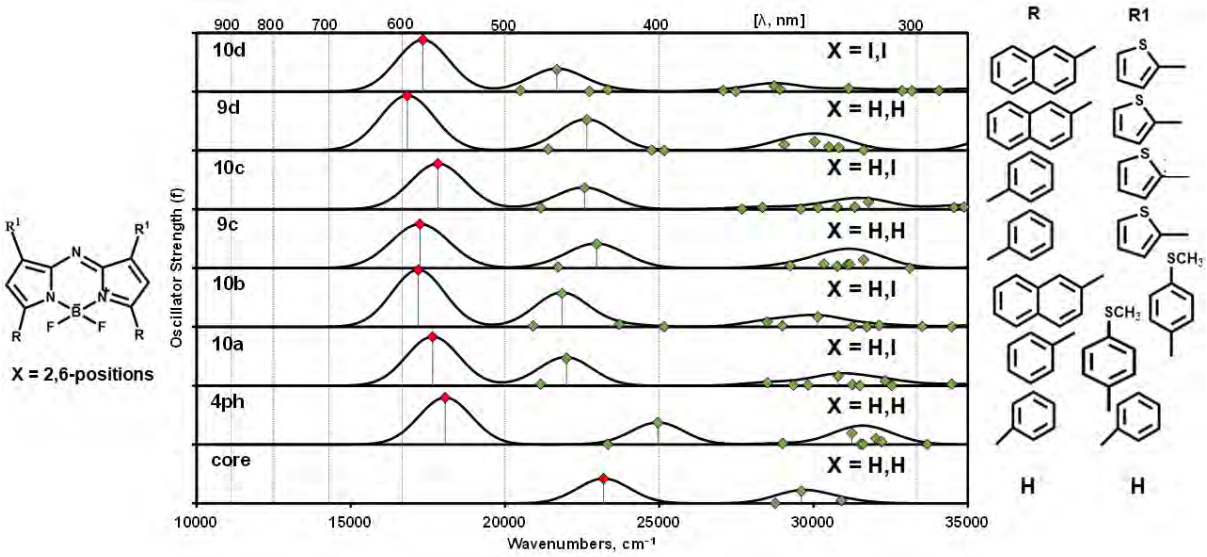

Figure 7.3: Calculated TD-DFT spectra for the B3LYP optimised geometries for aza-BODIPY dyes **9c-d** and **10a-d** and the **core** and **4Ph** model structures at the CAM-B3LYP/SDD level of theory. The red diamonds highlight the main visible region spectral band associated primarily with the $S_0 \rightarrow S_1$ one-electron transition. The simulated spectra were generated using the Chemcraft program with a fixed bandwidth of 2000 cm^{-1} [105]. The structures of the aza-BODIPY dyes are provided for easier identification of the structure-property relationships. R and R_1 rings on the right hand side correspond to those introduced at the positions indicated in the structure on the left hand side, while X refers to the 2,6-positions on the aza-BODIPY core.

7.3 Concluding remarks

The DFT and TD-DFT calculations were successfully conducted to establish the structure-property relationships across the series of related aza-BODIPY dyes. Trends identified in the calculations help to rationalise the spectroscopic properties that were observed experimentally and once the structure-property relationships are understood in this manner it is easier to rationally design novel dyes for applications.

CHAPTER 8

CONCLUSION AND FUTURE PROSPECTS

8. Conclusion

A series of structurally modified aza-BODIPY dyes were successfully synthesised and characterised for use in PACT and PDT activity studied. The iodinated aza-BODIPY dyes were synthesised following the five-step synthetic route:

(i) Aldol condensation of ketones and aldehyde to form a chalcone.

(ii) Base-catalysed Michael's addition of nitromethane to the chalcone under ethanolic reflux to form a nitromethane adduct.

(iii) Ethanolic reflux of the nitromethane adduct and ammonium acetate to form an aza-dipyrromethene.

(iv) Complexation of aza-dipyrromethene with BF_2 to form an aza-BODIPY.

(v) Iodination was accomplished using N-iodosuccinimide.

The aza-BODIPYs were characterised using UV-visible absorption spectroscopy, MALDI-TOF mass spectrometry, and ^{1}H NMR spectroscopy. The AuNPs and their nanoconjugates were characterised using UV-visible absorption spectroscopy, TEM, EDX spectroscopy, DLS, and XRD.

Aza-BODIPY dyes **9c-d** and **10a-d** and nanoconjugates **10a**-AuNPs and **10b**-AuNPs were all used in PACT activity studies against *S. aureus* and *E. coli*. **10a**-AuNPs and **10b**-AuNPs exhibited high antimicrobial activity with log reduction values of 9.41, while iodinated aza-BODIPYs **10a-d** also showed high antimicrobial activity with a log reduction of 8.94. In contrast, non-iodinated dyes exhibited low log reduction values of < 1, which demonstrates that the heavy iodine atoms and AuNPs had a significant antimicrobial effect since standard log reduction values > 3 mean that greater than

99.99% of the bacteria have been killed. This is the requirement stated by the Food and Drug Adminstration of the United States for a photosensitizer to be considered an effect antibacterial agent [106-108].

The *in vitro* photodynamic activities and dark cytotoxicities for aza-BODIPYs **9c-d** and **10c-d** were evaluated against human breast cancer MCF-7 cells. All the compounds exhibited minimal dark cytotoxicity with IC_{50} > 50 μM. After illumination, the iodinated compounds **10c** and **10d** exhibited moderately favourable PDT activities with IC_{50} values of 11.6 and 8.2 μM, respectively and < 30% cell viability at 50 μM, while non-iodinated dyes **9c** and **9d** had IC_{50} values of 12.5 and 19.2 μM, respectively, and exhibited < 40% cell viability at 50 μM, It is noteworthy that the differences in the IC_{50} values are relatively minor compared to what would be anticipated based on the Φ_{Δ} values in DMSO of 0.23 and 0.15 for **9c** and **9d** on the one hand, and 0.78 and 0.82 for **10c** and **10d** on the other. This suggests that more should be done to modify the structures enhance the uptake of **10c** and **10d**.

8.2 **Future work**

(i) A future goal will be enhanced aqueous solubility of the aza-BODIPY compound by introducing aryl substituents with nitrogen and sulfur atoms that can be quaternised and/or conjugated to nanoparticles for use in PDT (**Scheme 8.1**). Dyes of this type were reported recently by Mack and coworkers [94]. This work is already in progress but time constraints prevented its completion in time for inclusion in this thesis. The goal will be to compare the PDT activities of brominated and non-brominated compounds and the effect of introducing heavy atoms and quaternising nitrogen atoms.

(ii) The effect of conjugation to different types of nanoparticle on PDT and PACT activities, such as Ag, iron oxide, and Cu, that exhibit antimicrobial activity and improved necrosis or apoptosis [23,52,63], will be investigated.

(iii) The PDT studies for the **10a**-AuNP and **10b**-AuNP nanoconjugates that were not possible due to time constraints will be performed and PDT studies against Hela cells and MCF-7 breast cancer cells will be compared.

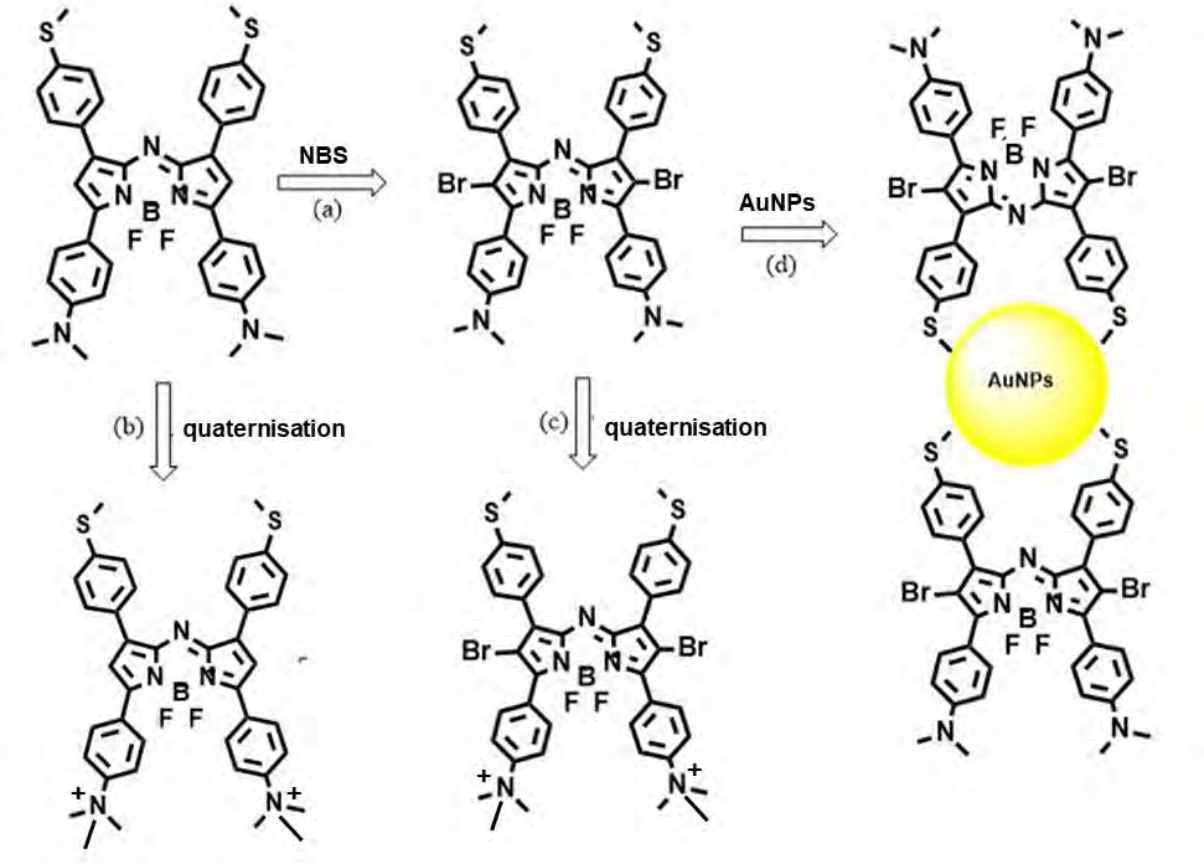

Scheme 8.1: Structures of the aza-BODIPYs to be explored by: (a) brominating the 2,6-positions to enhance the rate of ISC and thus increase the singlet oxygen quantum yield, (b) quaternising the dimethylamino group to improve solubility since aza-BODIPY have poor water solubility, (c) quaternising the brominated aza-BODIPY, and (d) conjugating brominated compounds

References

[1] M. Roser, F. Spooner, H. Ritchie, Our World in Data, (2018). https://ourworldindata.org/causes-of-death (Accessed: 16-02-2023)

[2] A. Moten, D. Schafer, M. Ferrari, Redefining global health priorities: Improving cancer care in developing settings, J. Glob. Health 1 (2014) 010304. https://doi.org/10.7189%2Fjogh.04.010304

[3] R. Stahel, J. Bogaerts, F. Ciardiello, D. de Ruysscher, P. Dubsky, M. Ducreux, S. Finn, P. Laurent-Puig, S. Peters, M. Piccart, E. Smit, C. Sotiriou, S. Tejpar, E. Van Cutsem, J. Tabernero, Optimising translational oncology in clinical practice: Strategies to accelerate progress in drug development, Cancer Treat. Rev. 41 (2015) 129–135. https://doi.org/10.1016/j.ctrv.2014.12.004.

[4] F. Bray, J. S. Ren, E. Masuyer, J. Ferlay, Global estimates of cancer prevalence for 27 sites in the adult population in 2008, Int. J. Cancer 132 (2013) 1133–1145. https://doi.org/10.1002/ijc.27711.

[5] N. Adarsh, R. R. Avirah, D. Ramaiah, Tuning Photosensitized Singlet Oxygen Generation Efficiency of Novel Aza-BODIPY Dyes, Org. Lett. 12 (2010) 5720–5723. https://doi.org/10.1021/ol102562k.

[6] P. Agostinis, K. Berg, K. A. Cengel, T. H. Foster, A. W. Girotti, S. O. Gollnick, S. M. Hahn, M. R. Hamblin, A. Juzeniene, D. Kessel, Photodynamic Therapy of Cancer: An Update, CA Cancer J Clin. 61 (2011) 250–281. https://doi.org/10.3322/caac.20114.

[7] M. Triesscheijn, P. Baas, J. H. M. Schellens, F. A. Stewart, Photodynamic Therapy in Oncology, Oncologist 11 (2006) 1034–1044. https://doi.org/10.1634/theoncologist.11-9-1034.

[8] C. A. Robertson, D. H. Evans, H. Abrahamse, Photodynamic therapy (PDT): A short review on cellular mechanisms and cancer research applications for PDT, J. Photochem. Photobiol. B 96 (2009) 1–8. https://doi.org/10.1016/j.jphotobiol.2009.04.001.

[9] D. Chen, Z. Zhong, Q. Ma, J. Shao, W. Huang, X. Dong, Aza-BODIPY-Based Nanomedicines in Cancer Phototheranostics, ACS Appl. Mater. Interfaces 12 (2020) 26914–26925. https://doi.org/10.1021/acsami.0c05021.

[10] G. Fan, L. Yang, Z. Chen, Water-soluble BODIPY and aza-BODIPY dyes: synthetic progress and applications, Front. Chem. Sci. Eng. 8 (2014) 405–417. https://doi.org/10.1007/S11705-014-1445-7.

[11] X. Li, J. Kim, J. Yoon, X. Chen, Cancer-Associated Stimuli-Driven Turn on Theranostics for Multimodality Imaging and Therapy, Adv. Mater. 29 (2017) 1606857. https://doi.org/10.1002/adma.201606857.

[12] I. Noh, D. Lee, H. Kim, C. Jeong, Y. Lee, J. Ahn, H. Hyun, J. Park, Y. Kim, Enhanced Photodynamic Cancer Treatment by Mitochondria-Targeting and Brominated Near-Infrared Fluorophores, Adv. Sci. 5 (2018) 1700481. https://doi.org/10.1002/advs.201700481.

[13] L. Li, Y. Chen, W. Chen, Y. Tan, H. Chen, J. Yin, Photodynamic therapy based on organic small molecular fluorescent dyes, Chinese Chem. Lett. 30 (2019) 1689–1703. https://doi.org/10.1016/j.cclet.2019.04.017.

[14] Y. Chen, L. Li, W. Chen, H. Chen, J. Yin, Near-infrared small molecular fluorescent dyes for photothermal therapy, Chinese Chem. Lett. 30 (2019) 1353–1360. https://doi.org/10.1016/j.cclet.2019.02.003.

[15] C. Hopper, Photodynamic therapy: a clinical reality in the treatment of cancer, Lancet Oncol. 1 (2000) 212–219. https://doi.org/10.1016/S1470-2045(00)00166-2.

[16] W. M. Sharman, C. M. Allen, J. E. van Lier, Photodynamic therapeutics: basic principles and clinical applications, Drug Discov. Today 4 (1999) 507–517. https://doi.org/10.1016/S1359-6446(99)01412-9.

[17] I. J. Macdonald, T. J. Dougherty, Basic principles of photodynamic therapy, J. Porphyrins Phthalocyanines 5 (2001) 105–129. https://doi.org/10.1002/jpp.328.

[18] T. Dai, B. B. Fuchs, J. J. Coleman, R. A. Prates, C. Astrakas, T. G. St. Denis, M.

S. Ribeiro, E. Mylonakis, M. R. Hamblin, G. P. Tegos, Concepts and Principles of Photodynamic Therapy as an Alternative Antifungal Discovery Platform, Front. Microbiol. 3 (2012) 1–16. https://doi.org/10.3389/fmicb.2012.00120.

[19] D. E. J. G. J. Dolmans, D. Fukumura, R. K. Jain, Photodynamic therapy for cancer, Nat. Rev. Cancer 3 (2003) 375–380. https://doi.org/10.1038/nrc1070.

[20] N. Mehraban, H. S. Freeman, Developments in PDT sensitizers for increased selectivity and singlet oxygen production, Materials 8 (2015) 4421–4456. https://doi.org/10.3390/ma8074421.

[21] J. Zhao, S. Ji, W. Wu, W. Wu, H. Guo, J. Sun, H. Sun, Y. Liu, Q. Li, L. Huang, Transition metal complexes with strong absorption of visible light and long-lived triplet excited states: From molecular design to applications, RSC Adv. 2 (2012) 1712–1728. https://doi.org/10.1039/c1ra00665g.

[22] S. S. Lucky, K. C. Soo, Y. Zhang, Nanoparticles in photodynamic therapy, Chem. Rev. 115 (2015) 1990–2042. https://doi.org/10.1021/cr5004198.

[23] B. G. Maiya, Photodynamic Therapy (PDT), Resonance 5 (2000) 6–18. https://doi.org/10.1007/bf02837901.

[24] S. B. Brown, E. A. Brown, I. Walker, The present and future role of photodynamic therapy in cancer treatment, Lancet Oncol. 5 (2004) 497–508. https://doi.org/10.1016/S1470-2045(04)01529-3.

[25] J. M. Ang, I. Bin Riaz, M. U. Kamal, G. Paragh, N. C. Zeitouni, Photodynamic therapy and pain: A systematic review, Photodiagnosis Photodyn. Ther. 19 (2017) 308–344. https://doi.org/10.1016/j.pdpdt.2017.07.002.

[26] P. Mroz, G. P. Tegos, H. Gali, T. Wharton, T. Sarna, M. R. Hamblin, Photodynamic therapy with fullerenes, Photochem. Photobiol. Sci. 6 (2007) 1139–1149. https://doi.org/10.1039/b711141j.

[27] J. Ma, L. Jiang, Photogeneration of singlet oxygen ($^1O_2$) and free radicals ($Sen^{\bullet-}$, $O_2^{\bullet-}$) by tetra-brominated hypocrellin B derivative, Free Radic. Res. 35 (2001) 767–777. https://doi.org/10.1080/10715760100301271.

[28] A. P. Castano, T. N. Demidova, M. R. Hamblin, Mechanisms in photodynamic therapy: Part One − Photosensitizers, photochemistry and cellular localization, Photodiagnosis Photodyn. Ther. 1 (2004) 279–293. https://doi.org/10.1016/S1572-1000(05)00007-4.

[29] K. Plaetzer, B. Krammer, J. Berlanda, F. Berr, T. Kiesslich, Photophysics and photochemistry of photodynamic therapy: Fundamental aspects, Lasers Med. Sci. 24 (2009) 259–268. https://doi.org/10.1007/s10103-008-0539-1.

[30] P. Agostinis, H. Breyssens, E. Buytaert, N. Hendrickx, Regulatory pathways in photodynamic therapy induced apoptosis, Photochem. Photobiol. Sci. 3 (2004) 721–729. https://doi.org/10.1039/b315237e.

[31] A. Casasa, G. Di Venosaa, T. Hasanb, A. Batlle, A. Casas, G. Di Venosa, T. Hasan, A. Batlle, Mechanisms of Resistance to Photodynamic Therapy, Curr. Med. Chem. 18 (2011) 2486–2515. https://doi.org/10.2174/092986711795843272.

[32] A. C. Trindade, J. A. P. De Figueiredo, L. Steier, J. B. B. Weber, Photodynamic Therapy in Endodontics: A Literature Review, Photomed. Laser Surg. 33 (2015) 175–182. https://doi.org/10.1089/pho.2014.3776.

[33] J. H. Correia, J. A. Rodrigues, S. Pimenta, T. Dong, Z. Yang, M. Wojcik, E. Preis, G. Litscher, pharmaceutics Photodynamic Therapy Review: Principles, Photosensitizers, Applications, and Future Directions, Pharmaceutics 13 (2021) 1332. https://doi.org/10.3390/pharmaceutics13091332.

[34] A. F. Dos Santos, D. R. Q. De Almeida, L. F. Terra, M. S. Baptista, L. Labriola, Photodynamic therapy in cancer treatment - an update review, J. Cancer Metastasis Treat. 5 (2019) 25. https://doi.org/10.20517/2394-4722.2018.83.

[35] P. Washer and H. Joffe. The "hospital superbug":Social representation of MRSA. Social Sci. Medicine 63 (2006) 2141–2152.

[36] M. Wainwright. Photodynamic antimicrobial chemotherapy (PACT), J. Antimicrob. Chemother. 42 (1998) 13–28. https://doi.org/10.1093/jac/42.1.13.

[37] M. R. Hamblin, T. Hasan, Photodynamic therapy: a new antimicrobial approach to infectious disease?, Photochem. Photobiol. Sci. 3 (2004) 436–450. https://doi.org/10.1039/b311900a.

[38] T. N. Demidova, M. R. Hamblin, Photodynamic Therapy Targeted To Pathogens, Int. J. Immunopathol. Pharmacol. 17 (2004) 245–254. https://doi.org/10.1177/039463200401700304.

[39] J. E. McGowan Jr, Antimicrobial resistance in hospital organisms and its relation to antibiotic use, Rev. Infect. Dis. 5 (1983) 1033–1048. https://doi.org/10.1093/clinids/5.6.1033

[40] F. F. Sperandio, Y. Huang, M. R. Hamblin, Antimicrobial Photodynamic Therapy to kill Gram-negative bacteria, Recent Pat. Antiinfect. Drug Discov. 8 (2013) 108–120. https://doi.org/10.2174/1574891x113089990012.

[41] H. Lu, J. Mack, Z. Shen, H. Lu, Structural modification strategies for the rational design of red / NIR region BODIPYs, Chem. Soc. Rev. 43 (2014) 4778–4823. https://doi.org/10.1039/c4cs00030g.

[42] J. Mack, T. Nyokong, TD-DFT calculations and MCD spectroscopy of porphyrin and phthalocyanine analogues : rational design of photosensitizers for PDT and NIR region sensor applications, Turkish J. Chem. 38 (2014) 1013–1026. https://doi.org/10.3906/kim-1406-32.

[43] P. M. Gurubasavaraj, V. P. Sajjan, B. M. Munoz-Flores, V. M. J. Perez, N. S. Hosmane, Recent advances in BODIPY compounds: synthetic mehods, optical and nonlinear optical properties, and their medical applications, Molecules 27 (2022) 1877. https://doi.org/10.3390/molecules27061877.

[44] J. H. Boyer, A. M. Haag, G. Sathyamoorthi, T. G. Pavlopoulos, Pyrromethene-BF_2 as Laser Dyes: 2, Heteroat. Chem. 4 (1993) 39–49. https://doi.org/10.1002/hc.520040107.

[45] A. Gorman, J. Killoran, C. O'Shea, T. Kenna, W. M. Gallagher, D. F. O'Shea, *In Vitro* Demonstration of the Heavy-Atom Effect for Photodynamic Therapy, J.

Am. Chem. Soc. 126 (2004) 10619–10631. https://doi.org/10.1021/ja047649e.

[46] T. Takemura, S.. Nakajima, N. Ohta, I. Sakata, S. Nakajima, I. Sakata, Critical Importance of the Triplet Lifetime of Photosensitizer in Photodynamic Therapy of Tumor, Photochem. Photobiol. 50 (1989) 339–344. https://doi.org/10.1111/J.1751-1097.1989.tb04167.x.

[47] S. O. McDonnell, D. F. O'Shea, Near-infrared sensing properties of dimethlyamino-substituted BF_2-azadipyrromethenes, Org. Lett. 8 (2006) 3493–3496. https://doi.org/10.1021/ol061171x.

[48] O. Buyukcakir, O. A. Bozdemir, S. Kolemen, S. Erbas, E. U. Akkaya, Tetrastyryl-BODIPY Dyes: Convenient Synthesis and Characterization of Elusive Near IR Fluorophores, Org. Lett. 11 (2009) 266–268. https://doi.org/10.1021/ol9019056.

[49] V. F. Donyagina, S. Shimizu, N. Kobayashi, E. A. Lukyanets, Synthesis of N,N-difluoroboryl complexes of 3,3′-diarylazadiisoindolylmethenes, Tetrahedron Lett. 49 (2008) 6152–6154. https://doi.org/10.1016/j.tetlet.2008.08.026.

[50] D. Wang, R. Liu, C. Chen, S. Wang, J. Chang, C. Wu, H. Zhu, E. R. Waclawik, Synthesis, photophysical and electrochemical properties of aza-boron-diquinomethene complexes, Dyes Pigments 99 (2013) 240–249. https://doi.org/10.1016/j.dyepig.2013.05.009.

[51] T. Kawawaki, Y. Negishi, H. Kawasaki, Photo/electrocatalysis and photosensitization using metal nanoclusters for green energy and medical applications, Nanoscale Adv. 2 (2020) 17–36. https://doi.org/10.1039/c9na00583h.

[52] Y. Cai, W. Si, W. Huang, P. Chen, J. Shao, X. Dong, Organic Dye Based Nanoparticles for Cancer Phototheranostics, Small 14 (2018) 1704247. https://doi.org/10.1002/smll.201704247.

[53] S. G. Awuah, Y. You, Boron dipyrromethene (BODIPY)-based photosensitizers for photodynamic therapy, RSC Adv. 2 (2012) 11169–11183. https://doi.org/10.1039/c2ra21404k.

[54] A. Bozdemir, L. T. Yildirim, E. Deniz, G. C. Isbasar, Bidirectional Switching of Near IR Emitting Boradiazaindacene Fluorophores, Org. Lett. 10 (2008) 3401–3403. https://doi.org/10.1021/ol801062h.

[55] Z. Ekmekci, M. D. Yilmaz, E. U. Akkaya, A Monostyryl-boradiazaindacene (BODIPY) Derivative as Colorimetric and Fluorescent Probe for Cyanide Ions, Org. Lett. 10 (2008) 461–464. https://doi.org/10.1021/ol702823u.

[56] A. Loudet, K. Burgess, BODIPY Dyes and Their Derivatives: Syntheses and Spectroscopic Properties, Chem. Rev. 107 (2007) 4891–4932. https://doi.org/10.1021/cr078381n.

[57] J. H. Gibbs, L. T. Robins, Z. Zhou, P. Bobadova-Parvanova, M. Cottam, G. T. Mccandless, F. R. Fronczek, M. G. H. Vicente, Bioorganic & Medicinal Chemistry Spectroscopic, computational modeling and cytotoxicity of a series of *meso*-phenyl and *meso*-thienyl-BODIPYs, Bioorg. Med. Chem. 21 (2013) 5770–5781. https://doi.org/10.1016/j.bmc.2013.07.017.

[58] R. P. Sabatini, T. M. McCormick, T. Lazarides, K. C. Wilson, R. Eisenberg, D. W. McCamant, Intersystem Crossing in Halogenated Bodipy Chromophores Used for Solar Hydrogen Production, J. Phys. Chem. Lett. 2 (2011) 223–227. https://doi.org/10.1021/jz101697y.

[59] M. A. T. Rogers, 156. 2:4-Diarylpyrroles. Part I. Synthesis of 2:4-diarylpyrroles and 2:2′:4:4′-tetra-arylazadipyrromethines, J. Chem. Soc. (1943) 590–596. https://doi.org/10.1039/jr9430000590.

[60] B. Knott, β-Cycloylpropionitriles. Part II. Conversion into *bis*-2-(5-cyclylpyrrole)azamethin salts, J. Chem. Soc. (1943) 1196–1201. https://doi.org/10.1039/jr9470001196.

[61] Y. Ge, D. F. O'Shea, Azadipyrromethenes: from traditional dye chemistry to leading edge applications, Chem. Soc. Rev. 45 (2016) 3846–3864. https://doi.org/10.1039/c6cs00200e.

[62] M. J. Hall, S. O. McDonnell, J. Killoran, D. F. O'Shea, A Modular Synthesis of

Unsymmetrical Tetraarylazadipyrromethenes, J. Org. Chem. 70 (2005) 5571–5578. https://doi.org/10.1021/jo050696k.

[63] S. R. Mudshinge, A. B. Deore, S. Patil, C. M. Bhalgat, Nanoparticles: Emerging carriers for drug delivery, Saudi Pharm. J. 19 (2011) 129–141. https://doi.org/10.1016/j.jsps.2011.04.001.

[64] G. Aygar, M. Kaya, N. Ozkan, S. Kocabiyik, M. Volkan, Preparation of Silica Coated Cobalt Ferrite Magnetic Nanoparticles for the Purification of Histidine-tagged Proteins, J. Phys. Chem. Solids 87 (2015) 64–71. https://doi.org/10.1016/j.jpcs.2015.08.005.

[65] N. Rapulenyane, E. Antunes, T. Nyokong, A study of the photophysicochemical and antimicrobial properties of two zinc phthalocyanine-silver nanoparticle conjugates, New J. Chem. 37 (2013) 1216–1223. https://doi.org/10.1039/c3nj41107a.

[66] O. J. Achadu, T. Nyokong, Application of graphene quantum dots functionalized with thymine and thymine-appended zinc phthalocyanine as novel photoluminescent nanoprobes, New J. Chem. 41 (2017) 1447–1458. https://doi.org/10.1039/c6nj03285k.

[67] S. Tran, P. J. Degiovanni, B. Piel, P. Rai, Cancer nanomedicine: a review of recent success in drug delivery, Clin. Transl. Med. 6 (2017) e44. https://doi.org/10.1186/s40169-017-0175-0.

[68] R. Singh, J. W. Lillard Jr, Nanoparticle-based targeted drug delivery, Exp. Mol. Pathol. 86 (2009) 215–223. https://doi.org/10.1016/j.yexmp.2008.12.004.

[69] A. Albanese, P. S. Tang, W. C. W. Chan, The Effect of Nanoparticle Size, Shape, and Surface Chemistry on Biological Systems, Annu. Rev. Biomed. Eng. 14 (2012) 1–16. https://doi.org/10.1146/annurev-bioeng-071811-150124.

[70] Y. Xin, M. Yin, L. Zhao, F. Meng, L. Luo, Recent progress on nanoparticle-based drug delivery systems for cancer therapy, Cancer Biol. Med. 14 (2017) 228–241. https://doi.org/10.20892/j.issn.2095-3941.2017.0052.

[71] A. Assuncão, B. Vieira, J. P. Lourenço, M. C. Costa, Recovery of gold(0) nanoparticles from aqueous solutions using effluents from a bioremediation process, RSC Adv. 6 (2016) 5–32. https://doi.org/10.1039/c6ra24503j.

[72] M. Tintoré, S. Mazzini, L. Polito, M. Marelli, A. Latorre, Á. Somoza, A. Aviñó, C. Fàbrega, R. Eritja, Gold-Coated Superparamagnetic Nanoparticles for Single Methyl Discrimination in DNA Aptamers, Int. J. Mol. Sci. 16 (2015) 27625–27639. https://doi.org/10.3390/ijms161126046.

[73] C. Lok, C. Ho, R. Chen, Q. He, W. Yu, H. Sun, P. K. Tam, J. Chiu, C. Che, Proteomic Analysis of the Mode of Antibacterial Action of Silver Nanoparticles, J. Proteome Res. 2 (2006) 916–924. https://doi.org/10.1021/pr0504079.

[74] B. X. Huang, S. Neretina, M. A. El-Sayed, Gold Nanorods: From Synthesis and Properties to Biological and Biomedical Applications, Adv. Mater. 21 (2009) 4880–4910. https://doi.org/10.1002/adma.200802789.

[75] P. Calzavara-Pinton, M. Rossi, S. Raffaella, V. Marina, Photodynamic Antifungal Chemotherapy, Photochem. Photobiol. 88 (2012) 512–522. https://doi.org/10.1111/j.1751-1097.2012.01107.x.

[76] A. Rai, C. C. Perry, Antibiotic mediated synthesis of gold nanoparticles with potent antimicrobial activity and their application in antimicrobial coatings, J. Mater. Chem. 20 (2010) 6789–6798. https://doi.org/10.1039/c0jm00817f.

[77] E. B. Dickerson, E. C. Dreaden, X. Huang, I. H. El-Sayed, H. Chu, S. Pushpanketh, J. F. McDonald, M. A. El-Sayed, Gold nanorod assisted near-infrared plasmonic photothermal therapy (PPTT) of squamous cell carcinoma in mice, Cancer Lett. 269 (2008) 57–66. https://doi.org/10.1016/j.canlet.2008.04.026.

[78] T. P. Mthethwa, S. Tuncel, T. Nyokong, Photophysical and photochemical properties of a novel thiol terminated low symmetry zinc phthalocyanine complex and its gold nanoparticles conjugate, Dalton Trans. 42 (2013) 4922–4930. https://doi.org/10.1039/c3dt32698e.

[79] R. Ranganathan, S. Madanmohan, A. Kesavan, G. Baskar, Y. R. Krishnamoorthy, R. Santosham, D. Ponraju, S. K. Rayala, G. Venkatraman, Nanomedicine: Towards development of patient-friendly drug-delivery systems for oncological applications, Int. J. Nanomedicine 7 (2012) 1043–1060. https://doi.org/10.2147/ijn.s25182.

[80] R. C. Soy, B. Babu, J. Mack, T. Nyokong, The photodynamic activities of the gold nanoparticle conjugates of phosphorus(V) and gallium(III) A_3 *meso*-triarylcorroles, Dyes Pigments 194 (2021) 109631. http://dx.doi.org/10.1016/j.dyepig.2021.109631

[81] Z. Shi, X. Han, W. Hu, H. Bai, B. Peng, L. Ji, Q. Fan, L. Li, W. Huang, Bioapplications of small molecule Aza-BODIPY: from rational structural design to *in vivo* investigations, Chem. Soc. Rev. 49 (2020) 7533–7567. https://doi.org/10.1039/d0cs00234h.

[82] S. Fery-Forgues, D. Lavabre, Are Fluorescence Quantum Yields So Tricky to Measure? A Demonstration Using Familiar Stationery Products, J. Chem. Educ. 76 (1999) 1260–1264. https://doi.org/10.1021/ed076p1260.

[83] R. O. Ogbodu, T. Nyokong, The effect of ascorbic acid on the photophysical properties and photodynamic therapy activities of zinc phthalocyanine-single walled carbon nanotube conjugate on MCF-7 cancer cells, Spectrochim. Acta A 151 (2015) 174–183. https://doi.org/10.1016/j.saa.2015.06.063.

[84] A. Ogunsipe, J. Chen, T. Nyokong, Photophysical and photochemical studies of zinc(ii) phthalocyanine derivatives-effects of substituents and solvents, New. J. Chem. 28 (2004) 822–827. https://doi.org/10.1039/B315319C.

[85] N. Nwahara, J. Britton, T. Nyokong, Improving singlet oxygen generating abilities of phthalocyanines: aluminum tetrasulfonated phthalocyanine in the presence of graphene quantum dots and folic acid, J. Coord. Chem. 70 (2017) 1601–1616. https://doi.org/10.1080/00958972.2017.1313975.

[86] M. Niedre, M. S. Patterson, B. C. Wilson, Direct Near-infrared Luminescence

Detection of Singlet Oxygen Generated by Photodynamic Therapy in Cells *In Vitro* and Tissues *In Vivo*, Photochem. Photobiol. 75 (2002) 382–391. https://doi.org/10.1562/0031-8655(2002)0750382dnildo2.0.co2

[87] F. Wilkinson, W. P. W. P. Helman, A. B. Ross, Quantum Yields for the Photosensitized Formation of the Lowest Electronically Excited Singlet State of Molecular Oxygen in Solution, J. Phys. Chem. Ref. Data 22 (1993) 113–262. https://doi.org/10.1063/1.555934.

[88] R. W. Redmond, J. N. Gamlin, A compilation of singlet oxygen yields from biologically relevant molecules, Photochem. Photobiol. 70 (1999) 391–475. https://doi.org/10.1111/j.1751-1097.1999.tb08240.x.

[89] M. R. Willcott, MestRe Nova, J. Am. Chem. Soc. 131 (2009) 13180. https://doi.org/ 10.1021/ja906709t.

[90] R. S. Riley, E. S. Day, Gold nanoparticle-mediated photothermal therapy: applications and opportunities for multimodal cancer treatment, Wiley Interdiscip. Rev. Nanomed. Nanobiotechnol. 9 (2017) e1449. https://doi.org/10.1002/wnan.1449.

[91] A. Sindelo, O. L. Osifeko, T. Nyokong, Synthesis, photophysicochemical and photodynamic antimicrobial chemotherapy studies of indium pyridyl phthalocyanines: Charge versus bridging atom, Inorg. Chim. Acta. 476 (2018) 68–76. https://doi.org/10.1016/j.ica.2018.02.020.

[92] D. O. Oluwole, C. M. Tilbury, E. Prinsloo, J. Limson, T. Nyokong, Photophysicochemical properties and *in vitro* cytotoxicity of zinc tetracarboxyphenoxy phthalocyanine − Quantum dot nanocomposites, Polyhedron 106 (2016) 92–100. https://doi.org/10.1016/j.poly.2015.12.060.

[93] B. Babu, E. Amuhaya, D. Oluwole, E. Prinsloo, J. Mack, T. Nyokong, Preparation of NIR absorbing axial substituted tin(iv) porphyrins and their photocytotoxic properties, MedChemComm 10 (2019) 41–48. https://doi.org/10.1039/c8md00373d.

[94] G. Kubheka, J. Mack, T. Nyokong, Z. Shen, NIR Absorbing AzaBODIPY Dyes for pH Sensing, Molecules 2020, 25, 3689. http://dx.doi.org/10.3390/molecules25163689

[95] N. Dubazana, Azadipyrromethenes for applications in photodynamic antimicrobial chemotherapy, photodynamic therapy and optical limiting, MSc thesis, Rhodes University, 2020.

[96] IsoPro, version 3.1; Cornell University. Software for MS analysis written by Michael W. Senko that implements Yergey's polynomial method.

[97] G. Ulrich, R. Ziessel, A. Harriman. The chemistry of fluorescent BODIPY dyes: versatility unsurpassed. Angew. Chem. Int. Ed. 47 (2008) 1184–1201. https://doi.org/10.1002/anie.200702070.

[98] L. V. Lutkus, S. S. Rickenbach, T. M. McCormick, Singlet oxygen quantum yields determined by oxygen consumption, J. Photochem. Photobiol. A 378 (2019) 131–135. https://doi.org/10.1016/j.jphotochem.2019.04.029.

[99] M. A. Bhosale, D. R. Chenna, R. Divya, J. P. Ahire, B. M. Bhanage. Morphological study of microwave-assisted facile synthesis of gold nanoflowers/nanoparticles in aqueous medium and their catalytic application for reduction of *p*-nitrophenol to *p*-aminophenol. RSC Adv. 5 (2015) 52817–52823. https://doi.org/10.1039/c5ra05731k

[100] M. V. Berridge, P. M. Herst, A. S. Tan, Tetrazolium dyes as tools in cell biology: New insights into their cellular reduction, Biotechnol. Annu. Rev. 11 (2005) 127–152. https://doi.org/10.1016/S1387-2656(05)11004-7.

[101] B. Babu, E. Prinsloo, J. Mack, T. Nyokong, Synthesis, characterization and photodynamic activity of Sn(IV) triarylcorroles with red-shifted Q bands, New J. Chem. 43 (2019) 18805–18812. https://dx.doi.org/10.1039/C9NJ03391B

[102] Gaussian 09, Revision E.01, M. J. Frisch, G. W. Trucks, H. B. Schlegel, G. E. Scuseria, M. A. Robb, J. R. Cheeseman, G. Scalmani, V. Barone, G. A. Petersson, H. Nakatsuji, X. Li, M. Caricato, A. V. Marenich, J. Bloino, B. G. Janesko, R.

Gomperts, B. Mennucci, H. P. Hratchian, J. V. Ortiz, A. F. Izmaylov, J. L. Sonnenberg, D. Williams-Young, F. Ding, F. Lipparini, F. Egidi, J. Goings, B. Peng, A. Petrone, T. Henderson, D. Ranasinghe, V. G. Zakrzewski, J. Gao, N. Rega, G. Zheng, W. Liang, M. Hada, M. Ehara, K. Toyota, R. Fukuda, J. Hasegawa, M. Ishida, T. Nakajima, Y. Honda, O. Kitao, H. Nakai, T. Vreven, K. Throssell, J. A. Montgomery, Jr., J. E. Peralta, F. Ogliaro, M. J. Bearpark, J. J. Heyd, E. N. Brothers, K. N. Kudin, V. N. Staroverov, T. A. Keith, R. Kobayashi, J. Normand, K. Raghavachari, A. P. Rendell, J. C. Burant, S. S. Iyengar, J. Tomasi, M. Cossi, J. M. Millam, M. Klene, C. Adamo, R. Cammi, J. W. Ochterski, R. L. Martin, K. Morokuma, O. Farkas, J. B. Foresman, and D. J. Fox, Gaussian, Inc., Wallingford CT, 2016.

[103] W. Chidawanyika, J. Mack, S. Shimizu, N. Kobayashi, T. Nyokong, Effect of peripheral fused ring substitution on the optical spectroscopy and electronic structure of metal phthalocyanine complexes, J. Porphyrins Phthalocyanines 13 (2009) 1053–1062. https://doi.org/10.1142/S1088424609001339.

[104] M. Shi, J. Tian, C. Mkhize, G. Kubheka, J. Zhou, J. Mack, T. Nyokong, Z. Shen, Synthesis, characterization and photodynamic therapy properties of an octa-4-tert-butylphenoxy-substituted phosphorus(V) triazatetrabenzcorrole, J. Porphyrins Phthalocyanines 18 (2014) 698–707. https://doi.org/10.1142/S1088424614500436.

[105] Chemcraft - graphical software for visualization of quantum chemistry computations. https://www.chemcraftprog.com (Accessed: 18-02-2023)

[106] L. Sobotta, P. Skupin-Mrugalska, J. Piskorz, J. Mielcarek, Non-porphyrinoid photosensitizers mediated photodynamic inactivation against bacteria, Dyes Pigments 163 (2019) 337–355. https://doi.org/10.1016/j.dyepig.2018.12.014.

[107] E. Alves, M.A. Faustino, M.G. Neves, A. Cunha, J. Tome, A. Almeida, An insight on bacterial cellular targets of photodynamic inactivation, Future Med. Chem. 6 (2014) 141–164. https://doi.org/10.4155/fmc.13.211.

[108] A. Spaeth, A. Graeler, T. Maisch, K. Plaetzer, CureCuma-cationic curcuminoids

with improved properties and enhanced antimicrobial photodynamic activity, Eur. J. Med. Chem. 159 (2017) 423–440. https://doi.org/10.1016/j.ejmech.2017.09.072.